UC San Diego

UC San Diego Electronic Theses and Dissertations

Title

Modeling the Structural and Mechanical Properties of Pulmonary Arteries in an Animal Model of Pulmonary Arterial Hypertension

Permalink

https://escholarship.org/uc/item/5mv4r2zb

Author

Pursell, Erica

Publication Date

2020

Peer reviewed|Thesis/dissertation

UNIVERSITY OF CALIFORNIA SAN DIEGO

Modeling the Structural and Mechanical Properties of Pulmonary Arteries in an Animal Model of Pulmonary Arterial Hypertension.

A thesis submitted in partial satisfaction of the
requirements for the degree
Master of Science

in

Bioengineering

by

Erica R. Pursell

Committee in charge:

Professor Daniela Valdez-Jasso, Chair
Professor Andrew McCulloch
Professor Jeff Omens

2020

The thesis of Erica R. Pursell is approved, and it is acceptable in quality and form for publication on microfilm and electronically:

_____

_____

_____

Chair

University of California San Diego

2020

DEDICATION

This thesis is dedicated to my family and friends. First, to my parents who believe and provide unlimited support in everything I do. They instilled in and showed me the benefits of a hard work ethic. Thank you to my aunts, uncles, and all the friends I have met along the way for your support and encouragement.

TABLE OF CONTENTS

LIST OF FIGURES

LIST OF TABLES

ACKNOWLEDGEMENTS

VITA

2020	M. S. in Bioengineering, University of California San Diego
2017	M. S. in Bioengineering, University of Illinois at Chicago
2015-2017	Graduate Teaching Assistant, University of Illinois, Chicago
2014	B. S. in Biomedical Engineering, University of Arizona
2014	B. S. in Mathematics, University of Arizona

PUBLICATIONS

Erica R. Pursell, Daniela Velez-Rendon, Daniela Valdez-Jasso, "Biaxial Properties of the Left and Right Pulmonary Arteries in a Monocrotaline Rat Animal Model of Pulmonary Arterial Hypertension", *Journal of Biomechanical Engineering*, 138, 2016.

Daniela Velez-Rendon, **Erica R. Pursell**, Justin Shieh, Daniela Valdez-Jasso, "Relative Contributions of Matrix and Myocytes to Biaxial Mechanics of the Right Ventricle in Pulmonary Arterial Hypertension", *Journal of Biomechanical Engineering*, 141, 2019.

ABSTRACT OF THE THESIS

Modeling the Structural and Mechanical Properties of Pulmonary Arteries in an Animal Model of Pulmonary Arterial Hypertension.

by

Erica R. Pursell

Master of Science in Bioengineering

University of California San Diego, 2020

Professor Daniela Valdez-Jasso, Chair

Pulmonary arterial hypertension (PAH) is a progressive disease characterized by elevated mean pulmonary arterial pressure. Although the cause of the disease onset is unclear, manifestations such as remodeling and occlusion of the distal pulmonary arteries lead to pressure overload of the right ventricle, eventually leading to heart failure. While much research has focused on the remodeling of smooth muscle and endothelial cells in the pulmonary arteries, collagen extracellular matrix changes in structure and function are not well defined. In this thesis, mechanical and microstructural properties of pulmonary arteries were investigated during the progression of PAH. Results indicated that the axial and circumferential directions to not

respond the same to mechanical loading, collagen fibers become less tortuous and realign to a preferred direction, and left and right pulmonary arteries do not remodel identically. Five models of the pulmonary arterial mechanics were developed to determine the role of structural features in the vascular mechanical response found with biaxial tubular testing of vessels in a rat model of PAH. Models included families of fibers, viscoelasticity, and elasticity theory. While the viscoelasticity-based model was able to identify the changes in the vessel stiffness, it did not account for the structural changes undergone by the vessel. On the other hand, the fiber-family models were able to incorporate collagen fiber preferred directions but were either over-parameterized and or did not account for tortuosity and collagen diameter changes. The elasticity-based model was found to fit measured data, and identify differences in the modulus of elasticity found in circumferential and axial directional data. Future iterations of the model should include measurements such as individual fiber diameter, data from fibers throughout the vessel, or contributions from other vessel constituents such as elastin fibers.

1 Background and Significance

1.1 Pulmonary Arterial Hypertension

changes during disease progression directly affect pulmonary arterial tissue-level mechanical function. To test this hypothesis, we made detailed measurements of the pulmonary arterial collagen extracellular matrix architecture and multi-axial mechanical testing in a rat model of PAH. To relate the mechanical to structural properties, we then developed microstructure-motivated constitutive models.

1.2 Cellular Biology

PAH is a subcategory of pulmonary hypertension (PH) which has been known to occur in cases of medical conditions such as connective tissue disorder, indicating the importance of studying vascular components such as collagen [31, 59]. Molecular studies have further characterized changes in the extracellular matrix in PH. Namely, procollagen increases throughout pulmonary vascular walls with collagen and elastin accumulating in the media [43]. Other studies have investigated the contribution of cross-linking to the progression of pulmonary hypertension. For example, beta-aminopropionitrile (BAPN) has been used to prevent future cross-linking which alleviates PH, but does not reverse the disease [2, 51, 60, 61]. Additionally, several have noted the importance of adventitial fibroblasts in pulmonary hypertension, as their elevated activity

increases collagen content, fibronectin, and recruitment of macrophages as part of an inflammatory response [2, 40, 41, 54]. Adventitial fibroblasts can also differentiate into myofibroblasts, the principal producers of collagen and other extracellular matrix proteins [49], underlining the importance of understanding adaptations to the extracellular matrix in PAH.

While advances have been made to treat or prevent PH in rodent animal models, the same treatments have not been effective in treating human PAH. One example is inhibition of ASK1 which regulates apoptosis and is suggested to have an anti-fibrotic mechanism that decreases cardiac fibroblast activity, reducing ECM deposition [3]. Recently, inhibition of the mechanoactive feedback in PAH via YAP/TAZ-microRNA-13/301 in multiple cell types has been proven to ameliorate matrix remodeling and PH [2, 51]. However, such a disruption in the YAP/TAZ cascade has not been investigated in humans and the relationship between structural changes and vascular mechanical manifestations of PAH are not fully understood.

1.3   Vascular Mechanics

To investigate the structural contributions of collagen to vascular mechanics, groups have carried out uniaxial tests and histological studies, but few have investigated the anisotropic properties of the pulmonary vasculature via biaxial tests and even fewer have studied the biaxial properties of both the left and right pulmonary artery. For example, circumferential mechanical tests have demonstrated that left pulmonary arteries stiffen with hypoxia-induced PH (HPH) and recover in wild type mice when returned to normoxia, yet vessels further stiffen in mice resistant to collagen I degeneration [40, 56]. The recovery of animals in HPH emphasizes the dynamical response of tissues and the importance of collagen in this model as an acute form of PH. On the other hand, Huang *et al.* only determined the incremental Young's modulus of the left pulmonary artery in the axial direction but noted that the vessel responds different axially than circumferentially [26]. However, the left and right pulmonary arteries serve unequal lobes

of lungs [8, 55], the percent blood flow received by the left pulmonary artery is about half that of the right pulmonary artery [45, 46], and blood vessels are known to have strong mechanical interactions between axial and circumferential axes, underlining the importance of studying the mechanics of both axes in both arteries.

The importance of studying biaxial mechanics of arteries has been demonstrated in other arteries [28]. Therefore, biaxial studies are important to fully appreciate the remodeling process during PH. One of the first to present data on biaxial properties of pulmonary arteries, Debes and Fung, reported that in a planar biaxial system, healthy dog right pulmonary arteries behave differently axially than circumferentially [5]. However, this method requires flattening of samples which can induce artificial stresses. Similarly, Drexler *et al.* reported that under bubble inflation tests, rat pulmonary arteries are anisotropic and the mechanical response is not equal [6, 7]. Nonetheless, as with Debes and Fung, this method requires flattening of the tissue sample.

Recently, groups including ours have investigated pulmonary arterial mechanics in a tubular biaxial setting as an attempt to more closely match *in vivo* conditions. In our study, changes in pulmonary arterial mechanics differed both axially and circumferentially and between left and right pulmonary arteries [44]. However, conclusions were reached with a quasi-linear viscoelasticity model which did not explain how such changes arise. Contradictorily, Ramachandra and Humphrey did not find significant differences in the stiffness of mouse right and left pulmonary arteries [45]. However, they also noted that the microstructural model used in their study required more measured structural data to better predict vascular mechanics.

Others have incorporated methods of determining mechanical properties that do not require flattening samples, but also do not distinguish between axes. Such methods include atomic force microscopy and pressure-inflation tests of the arterial bed. In their AFM micro-indentation of vasculature, Liu *et al.* determined the stiffness of pulmonary arteries. Briefly, in the monocrotaline and sugen-hypoxia rat models of PAH, vessels stiffen prior to pressure levels reaching values indicative of PAH [33, 51]. Such results emphasize the importance of vascular mechanics in PAH.

However, care should be taken when interpreting results from AFM, since the probe shape can significantly impact measurements which are highly localized (measurements may be confused for representing the whole tissue) [48]. Not only has increased vascular stiffness been associated with increased collagen and fibronectin content, but pulmonary arterial cells cultured on stiffer matrices demonstrated increased proliferation, decreased apoptosis, exaggerated contraction of smooth muscle cells, and increased mRNA levels for lysyl oxidase, a cross-linking enzyme [33]. While collagen cross-linking has little effect on vascular stiffening at low load (up to 25 mmHg) [60], it appears to have a higher impact at higher pressures such as those seen in PH [61]. Such results emphasize the importance of the ECM in pulmonary arterial mechanics.

While the role of ECM remodeling in PH is increasingly appreciated, few attempts have been made to determine the relationship between microstructural and arterial stiffness in the pulmonary vasculature. Monson *et al.* used a 4-parameter Fung-type exponential constitutive model to model biaxial mechanics. However, stress-strain curves were difficult to fit since parameters tended toward unrealistic negative values [38]. In a later study, Tian *et al.* used a constitutive model incorporating collagen content, cross-linking, and elastin content. Here, they found that elastin did not change in PH, but collagen content was well correlated with its parameter and cross-linking moderately correlated with its parameter [53]. These differences further demonstrate the importance of collagen content to pulmonary mechanics.

1.4   Collagen Fiber Architecture and Morphology

In addition to collagen content, vascular mechanics have been associated with collagen organization and structure such as diameter and tortuosity. In their study, Tian *et al.* found that while fibers were oriented in all directions, the majority of the fibers were oriented circumferentially [53]. Assuming all fibers behave similarly, these findings would suggest the circumferential direction to exhibit greater stiffness. Attempts to verify such a relationship

between fiber orientation and vascular mechanics have been made in the aorta and carotid artery [10, 11, 17, 23, 24, 42]. Briefly, these studies present models which lump fibers into two and four fiber families. Nonetheless, a major limitation to these studies is the over-parameterization of the problem set. For this reason, Ramachandra and Humphrey have suggested to use measured stress, material stiffness, and stored energy to compare biaxial results until more structural data are available to construct a more complete structural model [45]. Additionally, these studies assume equal weight for contributions from each of the fiber families, which has not been confirmed. In a later study, Gasser *et al.* incorporated a Bingham distribution function in their model to determine the effect of fiber distribution on wall mechanics of abdominal aortic aneurysms (AAA). While they were able to link fiber orientation and anisotropy of the AAA wall, they neglected to investigate the dependence of collagen mechanical properties on collagen fiber undulation [18]. Furthermore, our group observed a change of *collagen orientation and structure* in the right pulmonary artery of rats injected with monocrotaline [44]. Therefore, measured microstructural properties should be included in constitutive models of pulmonary vascular mechanics and could help to identify the structural changes during PAH that are most important in determining the altered mechanical properties that result from PAH remodeling.

1.5   Specific Aims

The overall goal of the work is to use microstructurally-based mathematical models of the pulmonary arteries, in conjunction with structural measurements of the collagen matrix, to determine how the extracellular matrix contributes to changes in mechanical function of the vessels.

Aim 1: Investigate the mechanical and structural properties of the pulmonary arteries in PAH.

We hypothesize that the structural properties change with the progression of the disease, affecting the mechanical properties of the pulmonary arteries. To test our hypothesis, we will carry out biaxial mechanical tests and quantify the architecture and morphology of the collagen extracellular matrix at different stages of the disease via second harmonic generation (SHG) using a multiphoton microscope. Data collected from vascular mechanics are fitted with a model that determines the time-dependence and stiffness of pulmonary arteries.

Aim 2: Develop microstructurally motivated constitutive model of pulmonary arteries during the progression of PAH.

We hypothesize that the changes in structural properties of the collagen extracellular matrix during PAH remodeling will affect the pulmonary vascular tissue biaxial mechanics. To test this hypothesis, we first seek to identify the differences in mechanical properties of the left and right pulmonary arteries given their difference in collagen fiber orientations. To incorporate how the collagen fiber architecture and morphology contribute to the wall properties, we used structurally-motivated constitutive models of family of fibers and elasticity theory.

2 Methods

In this Chapter, we describe how the disease is induced and confirmed in animals, how the tissues are prepared for mechanical testing and structural quantification, the mechanical testing protocols, data processing, and constitutive model derivation and numerical implementation.

2.1 Animal Model of PAH

The animal models of PAH that most closely replicate plexiform lesions in patients with PAH are induced through exposure to hypoxia, a combination of sugen and hypoxia (SuHx), monocrotaline (MCT) and a combination of MCT lung pneumonectomy. In the hypoxia model, the animals are exposed to hypoxic conditions with oxygen levels of at 10% for 10 days to 3 weeks [7, 29, 40, 41, 43, 56, 60, 61]. However, animals in this model recover after returning to normoxia [40, 41, 56]. Furthermore, the hypoxia-induced model of PH does not form the plexiform lesions seen in human cases of PAH [21]. Sugen-hypoxia is a more recent model of PAH where animals are injected with a vascular endothelial growth factor receptor blocker prior to entering a hypoxia chamber for three weeks. Animals are then returned to normoxia where their disease progresses to a severe state.

Here, we used the MCT animal model of PAH in male Sprague Dawley rats. MCT causes endothelial cell injury, increased pulmonary arterial pressure, and RV hypertrophy that occurs 3-4 weeks after injection [21, 37]. In this model, the drug crotaline is injected subcutaneously in

animals and is activated in the liver, becoming an endothelial toxin [21, 62].

Monocrotaline is prepared by dissolving crotaline powder (C2401-1G Sigma-Aldrich, St. Louis, MO) in 1 M and adjusting the to 7.0 with 0.1 M NaOH. This yielded a final solution of 0.025 g/ml to inject rats with a dose of 60 mg/kg. To study the effects of injection, a placebo solution was prepared by neutralizing the PH of 1 M HCl with 0.1 M NaOH. This solution was injected at volumes matching that of a 60 mg/kg dose of MCT and used as a control group. Animals were then studied at 1, 2, 3, and 4 weeks post-injection.

2.2   Tissue Collection Preparation

Prior to tissue harvesting, an open chest surgery was performed to measure *in vivo* hemodynamics to confirm the hypertensive state of the animals. Here, right ventricular blood pressure and volume, and pulmonary pressure are measured as described by Gerringer *et al.* [20]. Briefly, animals were anesthetized with oxygen and 4% isoflurane, intubated, and placed on a ventilator (SAR-1000 Ventilator, CWE Inc., Ardmore, PA, USA). A 1.6F dial pressure sensor catheter (Transonic Scisence, Ontario, Canada) was inserted to the RV and through the pulmonic valve such that RV and and pulmonary arterial pressure could both be measured.

Following hemodynamic measurements, the animals are exsanguinated and the lungs flushed with a phosphate buffered saline (PBS) and heparin mixture to prevent clotting and remove blood. The heart and lungs are then isolated from the rat by carefully disconnecting the lungs from the surrounding chest walls and diaphragm via blunt dissection. Five vessels are also severed to remove the heart-lung complex: right/right anterior vena cava, caudal vena vaca, the ascending aorta, and a vessel that crosses over the descending aorta. Finally, the trachea is severed and used to grip the heart and lungs while removing from the chest, continuing blunt dissections to clear any connective tissues. Special care was taken when cutting ligamentum arteriosum (connection between the pulmonary artery and aorta where the ductus arteriosis was). After
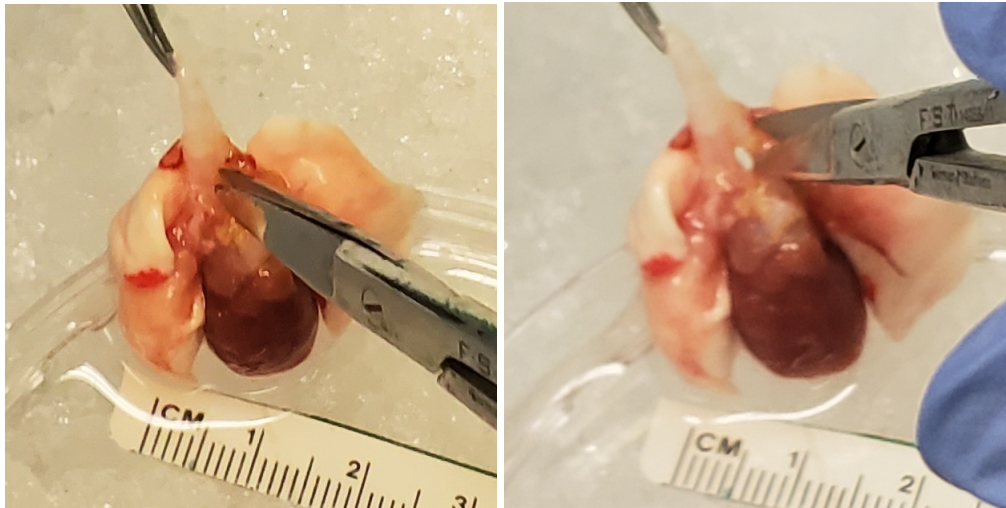
Figure 2.1: Identifying the bifurcation of the trachea by holding the trachea with forceps and using blunt dissections to separate the branching segments (Left). After the branching segments are identified, they are carefully cut so the trachea can be removed (Right).

successful removal, the heart and lungs were placed in a petri dish for isolating the pulmonary arteries.

To begin separating the two lungs, the bifurcation in the remaining trachea is first identified with blunt dissections. The two branching bronchi are then cut and the trachea segment discarded (Figure 2.1). Next, the main pulmonary artery is identified as the vessel adjacent to the aorta and cut along the interface with the RV. A cannula is then carefully placed through the MPA to trace the vessels (Figure 2.2). Once the locations of the PAs were determined, the veins (translucent and slightly yellow in appearance) were cut to complete the separation of lungs and heart (with the exception of the pulmonary arteries remaining the only connection between the lungs).

Once the cannula was directed into the LPA, the extralobar segment of the vessel is cleared of any material so that the LPA was plainly visible. The cannula is then redirected to the RPA and the left lung removed by cutting the LPA at the bifurcation of the MPA. After ensuring that the cannula entered the largest lobe of the right lung, the other lobes are removed by cutting at their intersection with the cannulated RPA. For the final and largest lobe, the cannulated artery is exposed by both cutting about 2 millimeters away from where the cannula should be and by
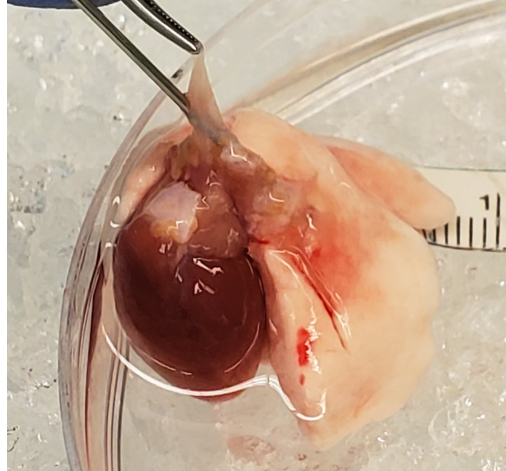
Figure 2.2: Here, a cannula is inserted in the main pulmonary artery to be used in guiding the dissection of the left and right pulmonary arteries.

using blunt dissection until the end of the cannula is reached (Figure 2.3). Here, the vessel is cut, allowing the cannula to exit the distal portion of the vessel. Curved forceps are then used to remove any remaining pleura.

Similarly to the last lobe of the right lung, the LPA is isolated from the pleura by first cannulating the LPA vessel, carefully cutting the lung about 2 millimeters away from where the cannula should be, blunt dissecting, and pulling pleura away until the cannulated LPA is exposed. In both lungs, the airways run parallel to the blood vessels. Therefore, closed scissors are often placed between the two and opened to identify any connecting points which are then severed.

After being isolated, the arteries are split into approximately 6 mm long segments and cannulated at each end using a blunt needle with an outer diameter closely matching the inner diameter of the vessel. To ensure the vessel does not slip off of the cannula, minimal amounts of glue (Permabond 240 High Viscosity, Ellsworth Adhesives, Germantown, WI) are placed at the edge of the vessel. Suture (Fine Science Tools Braided Silk Suture 5-0, Foster City, CA) lines are also tied near the ends of the vessel to mark the axial length (Figure 2.4). Finally, vessels are tested for leaks by closing one end of the vessel and pressurizing with air while the vessel is submerged in PBS. If any leaks exist at either end or due to holes from branching segments,
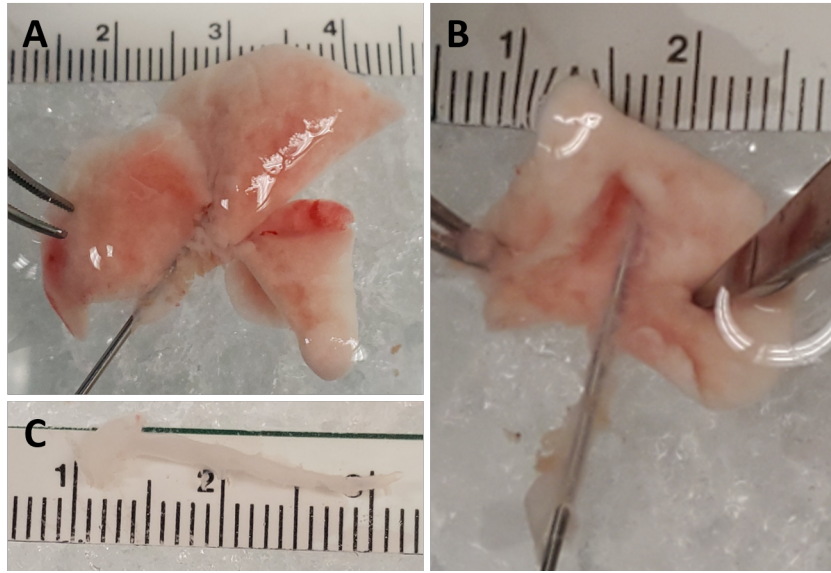
Figure 2.3: Right lung cannulated such that the cannula is directed into the largest lobe (A), Cannulated MPM and RPA with the smaller lobes of the right lung removed and the last and largest lobe split along the RPA (B), and the resulting MPA and RPA after dissection is complete (C).

~0.6 cm
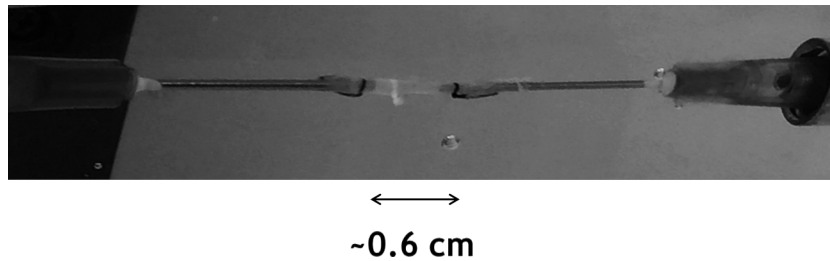
Figure 2.4: Vessel mounted in the tubular biax system with suture (black lines) denoting the ends of the vessel

minimal amounts of glue (so as not to impact the mechanical integrity of the vessel) are used to seal the leaks.

2.3   Mechanical Testing

Once cannulated, the segment was mounted in a Bose BioDynamic chamber (ElectroForce Mechanical Test Instruments, TA Instruments, New Castle, DE) tubular biaxial system. To mount the vessel, one end was first secured with the Luer-lock system of the cannula and tubular biax.

11
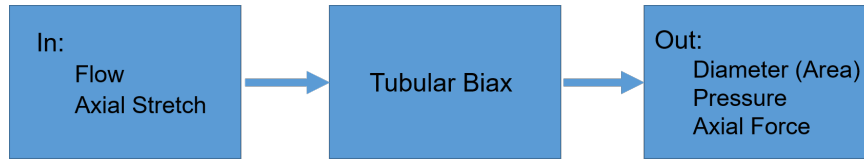
Figure 2.5: Approach used to mimic the *in vivo* conditions of the pulmonary arteries. Flow and axial stretch are the inputs chosen to match the pressures measured in the main pulmonary artery. Measurements taken are vessel outer diameter, pressure, and axial load.

The vessel was then twisted approximately one turn counter-clockwise so that the vessel would be straight when the second end was secured with it's Luer-lock system. Temperature-controlled PBS (approximately 37 °C) filled the chamber and was circulated through the vessel during each of two protocols: axial and circumferential. During the axial protocol, the vessel was exposed to a constant pressure matching the *in vivo* mPAP for the respective group while the vessel was cyclically stretched axially $\pm$ 5% of it's *in vivo* length at a rate of 10% of the *ex vivo* length per second. In the circumferential protocol, vessels were simultaneously subjected to cyclical pressures matching those measured *in vivo* and held at their *in vivo* length (stretched 40% of the *ex-vivo* length [30, 40, 60]). In each of the protocols, pressures were reached by adjusting the pump command (the flow) until pressure values matched those measured *in vivo*. While mechanically testing the vessels, the diameter was also tracked via a laser micrometer (Mitutoyo Corporation, Kawasaki, Japan) for use in stress and stretch calculations. A summary of the input and output parameters can be found in Figure 2.5 and examples of data collected can be found in Figures 2.6-2.7.

2.4   Mechanical Data Processing

Assuming thin-walled, incompressible vessels with no shear, circumferential θ and axial z Piola-Kirchhoff stress Π (Equations 2.4-2.8) and stretch λ (Equations 2.9-2.10) can be expressed as following the work of Humphrey and Delange [27] and Holzapfel [25], respectively and can be derived from Figure 2.8.
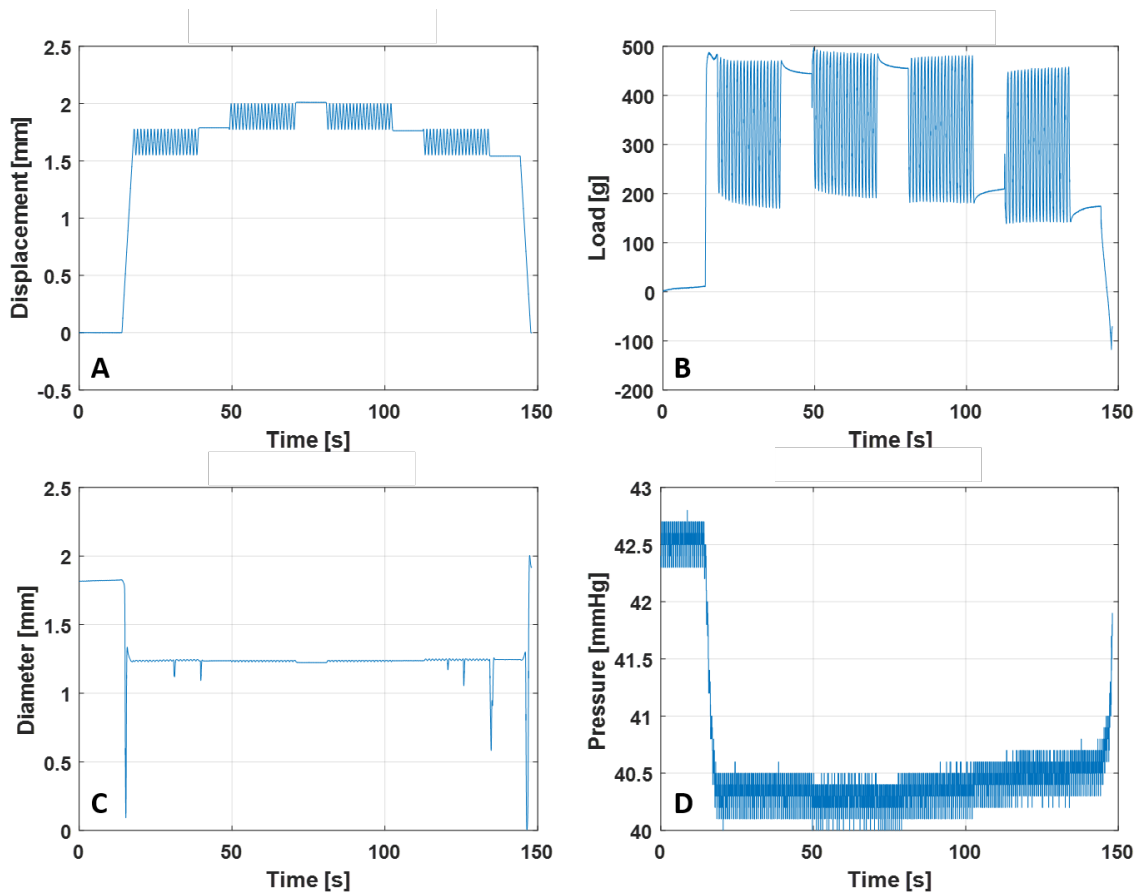
Figure 2.6: Data collected during the axial protocol. Here, axial displacement (A) is controlled and ranges between 35-40%, 40-45%, 45-40%, and 40-35% of the *ex vivo* length. Simultaneously, axial load (B) and vessel diameter (C) are measured. The flow rate is prescribed to reach a nearly constant intramural pressure (D).
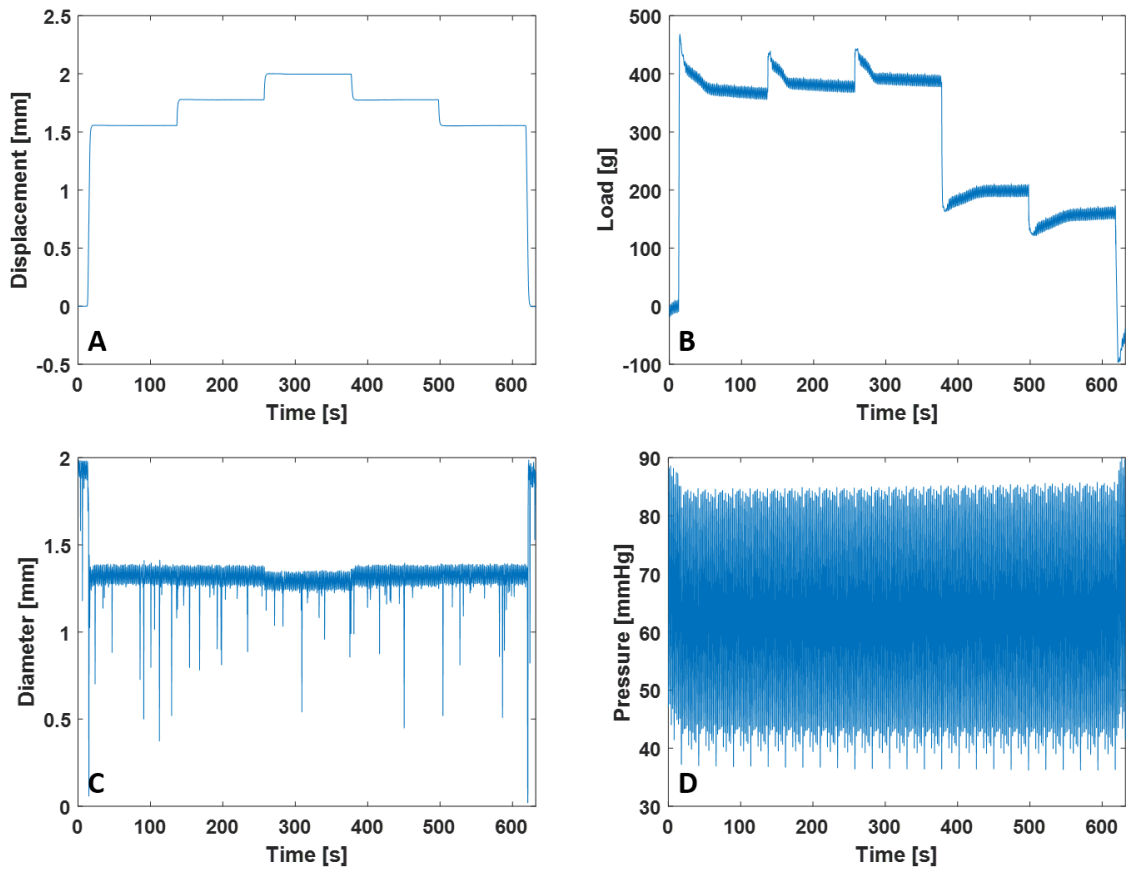
Figure 2.7: Data collected during the circumferential protocol. Here, axial load is held constant at 35%, 40%, 45%, 40%, and 35% of the *ex vivo* length (A). The axial load (B) and vessel diameter (B) are then measured during cyclical intramural pressure (D).
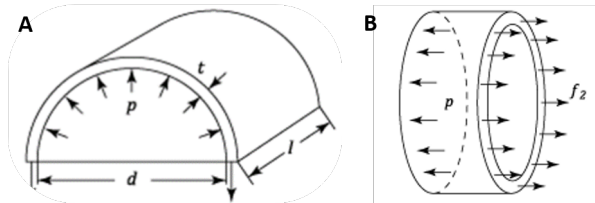
Figure 2.8: Representation of forces acting in circumferential direction (**A**) and axial direction (**B**) of a close-ended, pressurized vessel. Here, p is the internal pressure, d is the vessel diameter, l is the length of the vessel segment, t is the thickness of the vessel, and f_z is the axial force acting on the vessel.

Here, the forces must be balanced in the y-direction such that $\sum F_y = 0$. In the positive direction, we double integrate pressure from 0 to π and 0 to l to get the forces (f_p) acting upwards on the half segment of vessel by the pressure (Equation 2.1).

$$f_P = \int_0^l \int_0^\pi pr\sin\theta \, d\theta dl$$
$$= 2prl \tag{2.1}$$

In the negative direction, we have the internal forces of the tissue, which can be represented by circumferential stress (Π_θ) integrated over the area on which the force acts (Equation 2.2)

$$f_\theta = 2\int_0^l \int_r^{r+t} \Pi_\theta \, drdl$$
$$= 2lt\Pi_\theta \tag{2.2}$$

In equilibrium, these forces sum to zero:

$$\sum F_y = 0$$
$$= f_p + f_\theta$$
$$= 2prl + 2lt\Pi_\theta \tag{2.3}$$

Solving for circumferential stress, Equation 2.3 becomes

$$\Pi_\theta = \frac{pr}{t} \tag{2.4}$$

Similarly, the axial stress for a thin-walled, close-ended vessel can be derived from part B of Figure 2.8 by summing over forces in the x-direction. The forces acting in the negative

direction are the force due to axial stretch (f) and that due to pressure acting on the closed end of the cylinder ($f_{p,a}$), calculated as in Equation 2.5.

$$f_{p,a} = \int_0^r \int_0^{2\pi} pr \, d\theta dr$$
$$= \pi r^2 p$$

(2.5)

In the positive direction, we have the force f_2 due to the internal stress of the tissue:

$$f_2 = \int_0^{2\pi} r \int_r^{r+t} \Pi_z \, dr d\theta$$
$$= 2\pi r t \Pi_z$$

(2.6)

In equilibrium, the axial stretch force, force due to pressure, and force due to internal stress sum to zero:

$$\sum F_x = 0$$
$$= -f - f_{p,a} + f_2$$
$$= -f - \pi r^2 p + 2\pi r t \Pi_z$$

(2.7)

Solving for the internal axial stress, Equation 2.7 becomes

$$\Pi_z = \left(\frac{f}{2\pi r h} + \frac{pr}{2h} \right)$$

(2.8)

$$\lambda_\theta = \frac{r}{r_0}$$

(2.9)

$$\lambda_z = \frac{L}{L_0} \qquad (2.10)$$

where p is the internal pressure, r is the vessel radius, h is wall thickness, f is the axial force experienced by the vessel, r_0 is the cross-sectional vessel radius corresponding to the pressure before mechanical testing begins, L is the vessel length, and L_0 is the *ex-vivo* vessel length.

2.5 Constitutive Models

To relate stress and strain, several constitutive models were implemented. The first of which accounts for the dynamic loading and unloading effects of the vessels. The other models are structurally-motivated models informed by the organization of collagen fibers.

2.5.1 Quasi-linear Viscoelasticity Theory

To describe the time-varying pressure-diameter changes of the pulmonary vessels under cyclic conditions, we used the quasi-linear viscoelasticity (QLV) theory developed by Fung [15]. The QLV theory is used to model both the time- and history-dependent behavior of soft tissues through a convolution of a static elastic deformation response and time-invariant dynamics. The general formulation [44] is

$$\varepsilon_j(t) = \int_{-\infty}^{t} K(t-\gamma) s_j^{(e)}[F_j(\gamma)] \frac{ds_j^{(e)}[F_j(\gamma)]}{d\gamma} d\gamma \qquad (2.11)$$

Here, ε is the scalar quantity of vessel strain in the axial ($j = z$) and circumferential ($j = \theta$) directions, $K(t)$ is a creep function, and $s^{(e)}$ is function for a specified elastic response. To avoid numerical differentiation of experimental measurements, Equation 2.11 can be written in terms of an arbitrary time point, t_o:

$$\varepsilon_j(t) = K(0)s_j^{(e)}[F_j(t)] + \int_{t_o}^t [F_j(\gamma)]s_j^{(e)}\frac{dK(t-\gamma)}{d\gamma}d\gamma \tag{2.12}$$

With $K(t) = 1 - \sum_{i=1}^n C_i e^{-\frac{t}{b_i}}$.

For circumferential (θ) mechanics, F is the pressure in the vessel, while F is the axial load experienced by the vessel during axial mechanics and C_i is the amplitude associated with the relaxation time (b_i). The implementation of this QLV model was based on the work by Valdez-Jasso et al. [57] on human and ovine arteries. Here, vessels are assumed to be homogeneous, thin-walled, and incompressible. Therefore, pressure is uniformly distributed, and radial and shear stresses are negligible. Assuming the arteries are also elastic and orthotropic materials, the general linear elastic relation is

$$\varepsilon_{ij} = C_{ijkl}\Pi_{kl} \tag{2.13}$$

where $i, j, k, l = r, \theta, z$. Given our assumptions that shear and radial stresses are negligible (approximately zero), the linear elastic relation (Equation 2.13) reduces to the follow equations:

$$\varepsilon_\theta = \frac{1}{E_\theta}\Pi_\theta - \frac{\upsilon_{\theta z}}{E_z}\Pi_z \tag{2.14a}$$

$$\varepsilon_z = \frac{1}{E_z}\Pi_z - \frac{\upsilon_{\theta z}}{E_\theta}\Pi_\theta \tag{2.14b}$$

Here, Π is the normal stress tensor, ε is the strain tensor, υ is Poisson's ratio, and E is the elastic modulus.

With the initial load state (that before the test) as the reference configuration, circumferential (θ) and axial (z) strain (ε) can be computed as

$$\varepsilon_\theta = \frac{r - r_o}{r_o} \tag{2.15a}$$

$$\varepsilon_z = \frac{L - L_o}{L_o} \qquad (2.15b)$$

where r_o is vessel radius (r) and L_o is the vessel length (L) before mechanical testing began. Furthermore, under the initial load condition as the reference configuration, the axial strain is zero which reduces Equation 2.14a to

$$\varepsilon_\theta = \frac{1}{E_\theta}(\Pi_\theta - \upsilon_{z\theta}(\upsilon_{\theta z}\Pi_\theta)) = \frac{(1 - \upsilon_{z\theta}\upsilon_{\theta z})}{E_\theta}\Pi_\theta \qquad (2.16)$$

Similarly, the initial load condition as the reference configuration yields zero circumferential stress (cross-sectional area does not change due to constant pressure), reducing Equation 2.14b to

$$\varepsilon_z = \frac{1}{E_z}(\Pi_z - \upsilon_{\theta z}(\upsilon_{z\theta}\Pi_z)) = \frac{(1 - \upsilon_{\theta z}\upsilon_{z\theta})}{E_\theta}\Pi_z \qquad (2.17)$$

Substituting the circumferential stress (Equation 2.4) and strain (Equation 2.16) to Equation 2.14a, we can then write strain in terms of area:

$$1 - \sqrt{\frac{A_o}{A}} = \frac{r_o(1 - \upsilon_{z\theta}\upsilon_{\theta z})}{E_\theta h}p \qquad (2.18)$$

which allows us to write circumferential strain as

$$\varepsilon_\theta = \frac{r - r_o}{r} = 1 - \sqrt{\frac{A_o}{A}} \qquad (2.19)$$

Rearranging Equation 2.19, the cross-sectional area can be predicted as a function of time (Equation 2.20 and the linear elastic response in the circumferential direction implemented in the QLV framework becomes the expression in Equation 2.21.

$$A(t) = \frac{A_o}{(1 - \varepsilon_\theta(t))^2} \tag{2.20}$$

$$s_\theta^{(e)}[p(t)] = \frac{r_0(1 - \upsilon_{z\theta}\upsilon_{\theta z})}{E_\theta h} p \tag{2.21}$$

In the axial direction, the elastic response was described as in Equation 2.22 which could be related to axial lengthening by substituting into Equation 2.12, then substituting the resulting into Equation 2.15b and solving for length (Equation 2.23).

$$s_z^{(e)}[f(t)] = \frac{(1 - \upsilon_{\theta z}\upsilon_{z\theta})}{E_z} \Pi_z \tag{2.22}$$

$$L(t) = L_o(\varepsilon_z(t) + 1) \tag{2.23}$$

2.5.2 Microstructurally-motivated constitutive models

To account for the collagen structure and organization contributions to tissue response, we adapted the Fiber Family and the Elastica Models. A one-, two- and a four-fiber family model were used model the pulmonary vasculature.

Fiber Family Models

To better understand the relationship between collagen orientation and pulmonary mechanics, we used various fiber family models. These models depend on the orientation of collagen fibers within the tissue at an angle of α which is measured with respect to the axial direction. For these models, the deformation gradient was first determined.

To calculate the deformation gradient tensor, consider two configurations of a material in a real space $\mathbb{R}^3$: the reference and the current (deformed) configuration. Mapping an arbitrary

line segment in a material from the reference configuration d$\mathbf{X}$ to the current configuration d$\mathbf{x}$ requires the deformation gradient tensor, $\mathbf{F} = \frac{d\mathbf{x}}{d\mathbf{X}}$:

$$\mathbf{F} = \begin{bmatrix} \frac{dx_1}{dX_1} & \frac{dx_1}{dX_2} & \frac{dx_1}{dX_3} \\ \frac{dx_2}{dX_1} & \frac{dx_2}{d_X2} & \frac{dx_2}{dX_3} \\ \frac{dx_3}{dX_1} & \frac{dx_3}{dX_2} & \frac{dx_3}{dX_3} \end{bmatrix} \tag{2.24}$$

This deformation gradient tensor can then be used to determine the right Cauchy-Green deformation tensor ($\mathbf{C} = \mathbf{F}^T\mathbf{F}$) which can then be used to calculate stress. In the absence of shear, $\mathbf{F}$ is a diagonal tensor with the principle stretches as diagonal entries, which are radial (λ_r), circumferential (λ_θ), and axial (λ_z) stretches in cylindrical polar coordinates. Thus,

$$\mathbf{C} = \mathbf{F}^T\mathbf{F} = \begin{bmatrix} \lambda_r^2 & 0 & 0 \\ 0 & \lambda_\theta^2 & 0 \\ 0 & 0 & \lambda_z^2 \end{bmatrix} \tag{2.25}$$

The Cauchy-Green deformation tensor has three principle invariants, which are used to describe isotropic contributions to the strain energy density of a material and are independent of the coordinate system used. In the cylindrical polar coordinates, the first invariant is defined as follows:

$$I_1 = tr(\mathbf{C}) = \lambda_z^2 + \lambda_\theta^2 + \lambda_r^2 \tag{2.26}$$

In addition, there are pseudo-invariants of the right Cauchy-Green deformation tensor ($\mathbf{C}$) and $\mathbf{M} \otimes \mathbf{M}$ which can be used to incorporate anisotropic contributions. Such quantities are regarded as coordinate invariant and describe anisotropic qualities of materials through their dependence on $\mathbf{M}$, a preferred fiber direction generally defined in the reference configuration (Equation 2.27).

Because the invariant and pseudo-invariant quantities describe isotropic and anisotropic

properties of materials, they can then be used in the calculation of stress as done by Holzapfel *et. al.* (HGO model) [24]. In their study, Holzapfel *et. al.* introduced a two-fiber family model which incorporated contributions from the dominant fiber orientations in each the media and adventitia of rabbit carotid arteries. However, this model did not account for fibers in the axial and circumferential directions. Hence, Ferruzzi *et. al.* introduced a modified version of the HGO model in which the model was expanded to four fiber families [9]. In both of these models, only the first Cauchy invariant (Equation 2.26) and the fourth pseudo-invariant (Equation 2.28) are used with the directional unit vector for each family of fibers defined in Equation 2.27.

$$\mathbf{M}^i = \begin{bmatrix} 0 \\ sin(\alpha^i) \\ cos(\alpha^i) \end{bmatrix} \tag{2.27}$$

Here, *i* represents each of four fiber families and α^i are angles defined between the fiber and the axial direction. For the axial and circumferential directions, the angles are assigned values of $\alpha^1 = 0°$ and $\alpha^2 = 90°$, respectively whereas the third and fourth families of fibers are symmetrically oriented diagonal fibers with angles defined as $\alpha^3 = -\alpha^4 = \alpha$. See Figure 2.9 for a schematic of the fibers. Given this definition of the orientation vectors, the fourth pseudo-invariant can be expressed as follows:

$$IV^i = \mathbf{M}^i \cdot \mathbf{C}\mathbf{M}^i = \lambda_\theta^2 sin^2 \alpha^i + \lambda_z^2 cos^2 \alpha^i \tag{2.28}$$

The work done in a stress-strain relation for elastic materials only depends on strain whereas in hyperlastic materials (such as arteries), the work done is stored as potential energy in a thermodynamically reversible process. Additionally, in an elastic material, the stress-strain relation is path-independent whereas in hyperelastic materials, the relation is path dependent. Consequently, the need arises for a strain energy function.

Under hyperelastic theory, stress can be determined by taking the derivative a strain
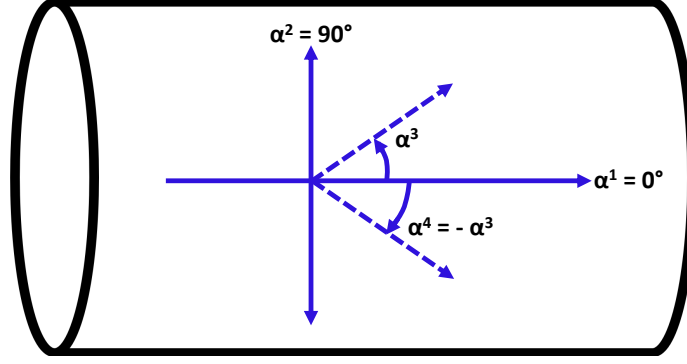
Figure 2.9: Schematic of the fiber families. Here, the horizontal line represents the axially oriented fibers ($\alpha^1 = 0°$), the vertical line represents the circumferentially oriented fibers ($\alpha^2 = 90°$), and the dashed lines represent the symmetrically oriented fibers ($\alpha^3 = -\alpha^4$).

energy density (work per unit volume) with respect to the deformation gradient tensor (**F**). This strain energy function (W) depends on the above-mentioned strain invariants and can be written as $W = W_{iso}(I_1) + W_{aniso}(IV)$ under the assumption that the strain-energy function describing the vessel's mechanics is a linear superposition of the isotropic (W_{iso}) and anisotropic (W_{aniso}) contributions. In this representation, the isotropic contribution solely depends on the first Cauchy invariant (Equation 2.26):

$$W_{iso} = \frac{c}{2}(I_1 - 3) \tag{2.29}$$

The anisotropic contribution is based on the Holzapfel, Gasser, Ogden (HGO) model, which incorporates two families of collagen fibers. This model is dependent on the orientation of the fiber families, indicated by the fourth pseudo-invariant of the right Cauchy-Green tensor.

$$W_{aniso} = \sum_{i=1}^{4} \frac{c_1^i}{4c_2^i}[e^{c_2^i(IV^i-1)^2} - 1] \tag{2.30}$$

With i representing the ith family of fibers. Each family of fibers is oriented in the reference configuration denoted by its respective unit vector ($\mathbf{M}^i$, defined in Equation 2.27). Summing Equations 2.29 and 2.30 and expanding, the strain energy function becomes:

$$W = \frac{c}{2}(I_1 - 3) + \frac{c_1^1}{4c_2^1}[e^{c_2^1(IV^1 - 1)^2} - 1]$$
$$+ \frac{c_1^2}{4c_2^2}[e^{c_2^2(IV^2 - 1)^2} - 1]$$
$$+ \frac{c_1^3}{4c_2^3}[e^{c_2^3(IV^3 - 1)^2} - 1] \tag{2.31}$$
$$+ \frac{c_1^4}{4c_2^4}[e^{c_2^4(IV^4 - 1)^2} - 1]$$

where I_1 is the first invariant of the right Cauchy-Green tensor (Equation 2.26) and IV is the fourth pseudo invariant of the right Cauchy-Green tensor (Equation 2.28). Assuming the pulmonary arteries are incompressible, the radial stretch can be re-written in terms of circumferential and axial stretches (Equation 2.32).

$$\lambda_r^2 = \frac{1}{\lambda_\theta^2 \lambda_z^2} \tag{2.32}$$

By enforcing incompressibility, Equation 2.26 then becomes Equation 2.33:

$$I_1 = \lambda_\theta^2 + \lambda_z^2 + \frac{1}{\lambda_\theta^2 \lambda_z^2} \tag{2.33}$$

Depending on the limitations of experimental designs, various stress calculations are required. For example, 1st Piola-Kirchhoff stress can be determined by the force on a body in the deformed configuration over the area of the body in it's reference configuration. Other forms of stress are Cauchy stress (force in the deformed state over area in the deformed state) and 2nd Piola-Kirchhoff stress (force in the reference state over area in the reference state). Because of experimentally obtained data, it is best to work with the 1st Piola-Kirchhoff stress which according to hyperelasticity theory, is determined through the following relation [25]:

$$P = -p\mathbf{F}^{-T} + \frac{\partial W(\mathbf{F})}{\partial \mathbf{F}} \tag{2.34}$$

where p is a Lagrange multiplier that enforces isovolumetric motions. Additionally, since our strain energy function is written in terms of the right Cauchy Strain tensor, it is more convenient to take the derivative of the strain energy function with respect to $\mathbf{C}$:

$$\frac{\partial W(\mathbf{F})}{\partial \mathbf{F}} = \frac{\partial W(\mathbf{C})}{\partial \mathbf{C}} \frac{\partial \mathbf{C}}{\partial \mathbf{F}} = 2\mathbf{F}\frac{\partial W(\mathbf{C})}{\partial \mathbf{C}} \tag{2.35}$$

Now, the derivative of the strain energy function (Equation 2.31) can be taken with respect to the Right Cauchy-Green tensor:

$$\frac{\partial W}{\partial \mathbf{C}} = \frac{c}{2}\mathbf{I} + \sum_{i=1}^{4} \frac{c_1^i}{4c_2^i} e^{c_2^i(IV^i-1)^2} 2c_2^i(IV^i - 1)\mathbf{M}^i\underline{\mathbf{I}}\mathbf{M}^i \tag{2.36a}$$

$$\mathbf{M}^i\underline{\mathbf{I}}\mathbf{M}^i = \begin{bmatrix} 0 & 0 & 0 \\ 0 & sin^2\alpha^i & cos\alpha^i sin\alpha^i \\ 0 & cos\alpha^i sin\alpha^i & cos^2\alpha^i \end{bmatrix} \tag{2.36b}$$

Combining Equations 2.36a and 2.36b, we get:

$$\frac{\partial W}{\partial \mathbf{C}} = \frac{c}{2}\mathbf{I} + \sum_{i=1}^{4} \frac{c_1^i}{2} e^{c_2^i(IV^i-1)^2}(IV^i - 1) \begin{bmatrix} 0 & 0 & 0 \\ 0 & sin^2\alpha^i & cos\alpha^i sin\alpha^i \\ 0 & cos\alpha^i sin\alpha^i & cos^2\alpha^i \end{bmatrix} \tag{2.37}$$

Plugging Equation 2.37 in to Equation 2.35 and substituting into Equation 2.34, the Cauchy stress can then be written as:

$$\mathbf{P} = -p\mathbf{F}^{-1} + \mathbf{F}[c\mathbf{I} + \sum_{i=1}^{4} c_1^i e^{c_2^i(IV^i-1)^2}(IV^i - 1)\mathbf{M}^i\underline{\mathbf{I}}\mathbf{M}^i] \tag{2.38}$$

25

Now, stress is:

$$
\begin{bmatrix} P_r & 0 & 0 \\ 0 & P_\theta & 0 \\ 0 & 0 & P_z \end{bmatrix} = -p \begin{bmatrix} \frac{1}{\lambda_r} & 0 & 0 \\ 0 & \frac{1}{\lambda_\theta} & 0 \\ 0 & 0 & \frac{1}{\lambda_z} \end{bmatrix} + c \begin{bmatrix} \lambda_r & 0 & 0 \\ 0 & \lambda_\theta & 0 \\ 0 & 0 & \lambda_z \end{bmatrix}
$$

$$
+ \sum_{i=1}^{4} \frac{c_1^i}{2} e^{c_2^i (IV^i - 1)^2} (IV^i - 1) \begin{bmatrix} 0 & 0 & 0 \\ 0 & \lambda_\theta sin^2\alpha^i & \lambda_\theta cos\alpha^i sin\alpha^i \\ 0 & \lambda_z cos\alpha^i sin\alpha^i & \lambda_z cos^2\alpha^i \end{bmatrix} \tag{2.39}
$$

Since the pulmonary arteries are assumed to be thin walled, the radial contributions of stress can be neglected, allowing for the Lagrange multiplier (p) to be solved (Equation 2.41) using Equation 2.40.

$$
P_r = 0 = -p \frac{1}{\lambda_r} + c\lambda_r \tag{2.40}
$$

$$
p = c\lambda_r^2 = \frac{c}{\lambda_\theta^2 \lambda_z^2} \tag{2.41}
$$

Plugging Equation 2.41 into Equation 2.39 results in the following measures of stress (Equations 2.42 and 2.43). Here, part b of Equations 2.42 and 2.43 are the simplified forms of part a. Note that fiber families 3 and 4 have been lumped together as discussed earlier.

$$
P_z = c \left(\lambda_z - \frac{1}{\lambda_\theta^2 \lambda_z^3} \right) + c_1^1 (IV^1 - 1) e^{c_2^1 (IV^1 - 1)^2} \lambda_z cos^2 0
$$

$$
+ c_1^2 (IV^2 - 1) e^{c_2^2 (IV^2 - 1)^2} \lambda_z cos^2 90 \tag{2.42a}
$$

$$
+ 2c_1^{3,4} (IV^{3,4} - 1) e^{c_2^{3,4} (IV^{3,4} - 1)^2} \lambda_z cos^2 \alpha
$$

$$P_z = c\left(\lambda_z - \frac{1}{\lambda_\theta^2 \lambda_z^3}\right) + c_1^1 (IV^1 - 1) e^{c_2^1 (IV^1 - 1)^2} \lambda_z$$
$$+ 2c_1^{3,4} (IV^{3,4} - 1) e^{c_2^{3,4} (IV^{3,4} - 1)^2} \lambda_z cos^2 \alpha \tag{2.42b}$$

$$P_\theta = c\left(\lambda_z - \frac{1}{\lambda_\theta^3 \lambda_z^2}\right) + c_1^1 (IV^1 - 1) e^{c_2^1 (IV^1 - 1)^2} \lambda_\theta sin^2 0$$
$$+ c_1^2 (IV^2 - 1) e^{c_2^2 (IV^2 - 1)^2} \lambda_\theta sin^2 90 \tag{2.43a}$$
$$+ 2c_1^{3,4} (IV^{3,4} - 1) e^{c_2^{3,4} (IV^{3,4} - 1)^2} \lambda_\theta sin^2 \alpha$$

$$P_\theta = c\left(\lambda_z - \frac{1}{\lambda_\theta^3 \lambda_z^2}\right) + c_1^2 (IV^2 - 1) e^{c_2^2 (IV^2 - 1)^2} \lambda_\theta$$
$$+ 2c_1^{3,4} (IV^{3,4} - 1) e^{c_2^{3,4} (IV^{3,4} - 1)^2} \lambda_\theta sin^2 \alpha \tag{2.43b}$$

Elastica Model

In previous implementations of the Elastica Model, collagen structural information contribute to uniaxial tissue mechanics [32, 34]. Here, fibers are assumed to be oriented in the same direction. However, the model can easily be adapted to account for fibers in at multiple directions within the tissue.

Collagen fibers from cardiac and aortic tissues have previously been modeled as helical and 2D corrugated spring structures to determine the relationship between collagen morphology and tissue mechanics [13, 32, 36]. While imaging of collagen fibers of cardiac tissues have revealed helical structures [13, 35], our MPM images (discussed in results) do not indicate such structures. Therefore, we chose to model the movement of fibers as 2D corrugated springs, following the work by Ling and Chow [32]. Under this assumption, fibers are assumed to have a sinusoidal waveform in which each quarter of a period can be treated as a bent rod (Figure 2.10). The force to deform this rod can be calculated as in Equation 2.44.
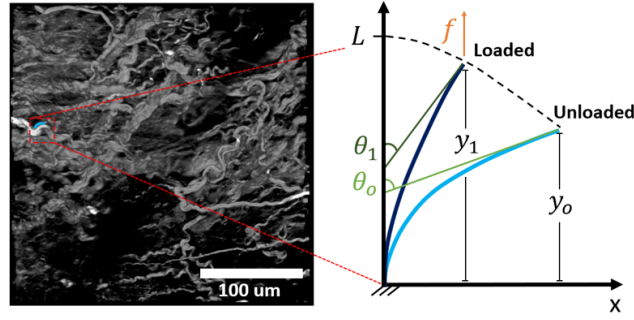
Figure 2.10: Schematic of a quarter period of fiber, modeled as a rod fixed at one end with the initial state unloaded and the final state loaded with a force f_1.

$$f_1 = \frac{EI}{2Ly_o} \int_0^{\theta_o} \frac{cos\theta d\theta}{\sqrt{cos\theta - cos\theta_o}} \int_0^{\theta_1} \frac{d\theta}{\sqrt{cos\theta - cos\theta_1}} \left[\frac{\sqrt{1 - cos\theta_o}}{\sqrt{1 - cos\theta_1}} - \frac{\int_0^{\theta_1} \frac{d\theta}{\sqrt{cos\theta - cos\theta_1}}}{\int_0^{\theta_o} \frac{d\theta}{\sqrt{cos\theta - cos\theta_o}}} \right] \quad (2.44)$$

Here, E is the Young's modulus of collagen, I is the moment area of a cylindrical rod, L is the length of a quarter period of the fiber, and y_o is the mid-line length of the quarter period. While L and y_o were measured from the MPM images, E can be determined through model optimization and I can be calculated from the measured diameter ($I = \frac{\pi D^4}{64}$). Finally, θ_o and θ_1 must be determined.

To find θ_o for a given tortuosity (T_o), the ratio of fiber length to mid-line length given by Equation 2.45 was solved using the *integral* function in MATLAB (version 9.6.0, Mathworks, Natick, MA) which numerically integrates a function with adaptive quadrature. Here, θ_o was initiated at 0.001 radians, and Equation 2.45 [32, 34] was evaluated and compared to the measured fiber tortuosity. If the difference between the two values was greater than 0.001, theta was increased by 0.001 radians and the function re-evaluated until either the difference between measured and calculated tortuosity was less than or equal to 0.001 or θ_o was greater than or equal to $\frac{\pi}{2}$ radians.

$$T_o = \frac{L}{y_o} = \frac{\int_0^{\theta_o} \frac{d\theta}{\sqrt{cos\theta - cos\theta_o}}}{\int_0^{\theta_o} \frac{cos\theta d\theta}{\sqrt{cos\theta - cos\theta_o}}} \tag{2.45}$$

Additionally, any given applied force had an accompanying fiber stretch (Equation 2.46) from which θ_1 can be determined via the same numerical integration method used for θ_o.

$$\begin{aligned}
\lambda_f &= \frac{y_1}{y_o} \\
&= \frac{L}{y_o} \frac{\int_0^{\theta_1} \frac{cos\theta d\theta}{\sqrt{cos\theta - cos\theta_1}}}{\int_0^{\theta_1} \frac{d\theta}{\sqrt{cos\theta - cos\theta_1}}}
\end{aligned} \tag{2.46}$$

Because the fiber stretch (λ_f) cannot be directly measured, it needs to be computed using the transformation of the stretch tensor $\mathbf{U}$ between the fiber and tissue coordinate systems in which we assume no rotation occurs due to our experimental setup:

$$\mathbf{U}_{f,c,r} = \mathbf{B}\mathbf{U}_{z,\theta,r}\mathbf{B}^T \tag{2.47}$$

With the stretch tensor in the fiber coordinate system ($\mathbf{U}_{f,c,r}$), the stretch tensor in the tissue coordinate system ($\mathbf{U}_{z,\theta,r}$), and the transformation matrix ($\mathbf{B}$) defined as follows [14]:

$$\mathbf{U}_{f,c,r} = \begin{bmatrix} \lambda_f & 0 & 0 \\ 0 & \lambda_c & 0 \\ o & 0 & \lambda_r \end{bmatrix}, \mathbf{U}_{z,\theta,r} = \begin{bmatrix} \lambda_z & 0 & 0 \\ 0 & \lambda_\theta & 0 \\ o & 0 & \lambda_r \end{bmatrix}, \text{ and } \mathbf{B} = \begin{bmatrix} cos\alpha & sin\alpha & 0 \\ -sin\alpha & cos\alpha & 0 \\ 0 & 0 & 1 \end{bmatrix} \tag{2.48}$$

So

$$\begin{bmatrix} \lambda_f & 0 & 0 \\ 0 & \lambda_c & 0 \\ 0 & 0 & \lambda_r \end{bmatrix} = \begin{bmatrix} \lambda_z cos^2\alpha + \lambda_\theta sin^2\alpha & (\lambda_\theta - \lambda_z)cos\alpha sin\alpha & 0 \\ (\lambda_\theta - \lambda_z)cos\alpha sin\alpha & \lambda_z sin^2\alpha + \lambda_\theta cos^\alpha & 0 \\ 0 & 0 & 1 \end{bmatrix} \qquad (2.49)$$

and therefore,

$$\lambda_f = \lambda_z cos^2\alpha + \lambda_\theta sin^2\alpha \qquad (2.50)$$

Now, to compare our model to measured mechanical data, we need to normalize the fiber force by dividing by the cross-sectional area of the tissue ($A_f = \frac{\pi D^2}{4}$). The resulting quotient is the tension in the fiber:

$$T_f = \frac{f_1}{A_{image}} \qquad (2.51)$$

This can then be transformed to the tissue coordinate system through the following:

$$\Pi_{z,\theta,r} = \mathbf{B}^T \Pi_{f,c,r} \mathbf{B} \qquad (2.52)$$

$$\begin{bmatrix} \Pi_z & 0 & 0 \\ 0 & \Pi_\theta & 0 \\ 0 & 0 & \Pi_r \end{bmatrix} = \begin{bmatrix} cos\alpha & -sin\alpha & 0 \\ sin\alpha & cos\alpha & 0 \\ 0 & 0 & 1 \end{bmatrix} \begin{bmatrix} T_f & 0 & 0 \\ 0 & 0 & 0 \\ 0 & 0 & 0 \end{bmatrix} \begin{bmatrix} cos\alpha & sin\alpha & 0 \\ -sin\alpha & cos\alpha & 0 \\ 0 & 0 & 1 \end{bmatrix} \qquad (2.53)$$

From here, we get the fiber contribution to stress in the axial (z) and circumferential (θ) directions of the tissue (Equation 2.54).

$$\Pi_z^f = T_f cos^2\alpha \qquad (2.54a)$$

30

$$\Pi_\theta^f = T_f sin^2\alpha \tag{2.54b}$$

The sum of all fiber stresses in each direction can then be scaled by a collagen area fraction (Equation 2.59)

$$T_f = \frac{f}{A_f} \tag{2.55a}$$

$$A_f = \frac{\pi D^2}{4} \tag{2.55b}$$

$$\Pi_z^f = T_f cos^2\alpha \tag{2.55c}$$

$$\Pi_{tiss,i} = AF_{col}\Pi_i^f \tag{2.55d}$$

The only remaining unknown variable is Young's modulus of elasticity E, which we assume is equal for all fibers in a given vessel.

2.6 Numerical Implementation

All numerical simulations were carried out in MATLAB. Due to varying sensitivity to starting points, two different minimization algorithms were implemented to find the global minima. The first algorithm was a direct-search algorithm based on the Nelder-Mead simplex and the other was a gradient-based method (nonlinear least-squares solver).

2.6.1 Quasi-linear Viscoelasticity Model

In order to solve the integral in the QLV model (Equation 2.12), a code using the trapezoidal rule was implemented. Here, the circumferential model was minimized against the measured area over time while the axial model was minimized against vessel length over time. For each of the directions, the elastic function was first optimized to obtain a good guess for

the inverse of the elastic modulus and either L_o (axial) or A_o (circumferential). The relaxation function was then added and the entire QLV function was optimized using the objective function defined in Equation 2.56. To minimize the objective function by adjusting the input parameters ($\phi_{ax} = \{E, C_1, b_1, L_o\}$ and $\phi_{circ} = \{A_0, E_\theta, C_1, b_1\}$), a direct search (Nelder-Mead simplex) method was implemented via the *fminsearch* function in MATLAB.

$$\hat{\phi} = argmin_\phi(J(\phi)) \tag{2.56a}$$

$$J(\phi) = \sqrt{\frac{\sum_{j=1}^{n}(X(t_j;\phi) - x_j)^2}{\sum_{j=1}^{n}x_j^2}} \tag{2.56b}$$

Here, X is the model prediction, x is the measured data, w is the set of parameters in a given model, and $\hat{\phi}$ is the set of optimal parameters. To find the minimum of the objective function, a Nelder-Mead algorithm was implemented with *fminsearch* function of MATLAB. A_o and L_o were based on the minimum cross-sectional area (mm^2) and vessel length of the individual data set, respectively. Although these parameters were measured, they entered the minimization algorithm for numerical stability purposes. The parameters E_θ and E_z were initially set to 4.8×10^6 mmHg, and $b_1 = 0.05$ s based on literature [57]. The product of the Poisson's ratios was arbitrarily chosen to be 0.25. In each case, parameters were constrained to positive values by taking the square root of the values before entering the optimization and squaring after exiting the optimizer. Additionally, C_1 was constrained to values between 0 and 1. To enforce this, γ was optimized and converted to C_1 (Equation 2.57).

$$C_1 = C_{1,max}\frac{\gamma^2}{1+\gamma^2} \tag{2.57}$$

2.6.2 Microstructurally-Motivated Models

Fiber Family Models

To begin incorporating structural information into the vascular wall mechanics, we used 1-, 2-, and 4-fiber family models. In each case, the process included a two-step optimization approach due to the imbalance of unknown parameters and known equations. First, the axial and circumferential data were each fitted to get a better initial guess for minimizing all parameters combined. While each model included the same isotropic contributions to stress, the anisotropic contributions varied depending on the number of fiber families considered.

One-fiber Family Model

The one-fiber family model accounts for fibers at a single dominant fiber orientation which was measured from multiphoton images of collagen taken at the center of the vessel wall. In total, this model has three parameters ($\phi = \{c, c_1^1, c_2^1\}$) that appear in the calculation of both axial and circumferential stress.

Two-fiber Family Model

In an attempt to separate axial and circumferential contributions to vessel mechanics, the two-fiber family model was also implemented. This model includes anisotropic contributions to stress from fibers oriented both axially and circumferentially and has 5 unknown parameters ($\phi = \{c, c_1, c_2^1, c_1^2, c_2^2\}$). Here, we assume that the contributions from fibers oriented between the axial and circumferential direction can be projected onto one of the two axes.

Four-fiber Family Model

To determine mechanical properties of the fibers oriented at a dominant angle between the axial and circumferential directions, we implemented a four-fiber family model. This model

included fibers oriented axially, circumferentially, and at two angles symmetrically oriented about the axial direction. Because these fibers are symmetrically oriented, their contributions to axial and circumferential mechanics are assumed equal, reducing the number of additional parameters by 2. In total, this model has seven unknown parameters ($\phi = c, c_1^1, c_2^1, c_1^2, c_2^2, c_1^{3,4}, c_2^{3,4}$). In our initial modeling efforts, α also entered the parameter optimization. However, the optimal angle did not vary from the guess (change in α did not affect the fitting of the model) and so α became fixed at its measured value.

General Optimization of Fiber Family Models

Initially, parameters were allowed to reach negative values to better fit the data. However, parameters related to stiffness became negative, which did not translate to physical interpretations. For these reasons, parameters were then constrained to positive values. To constrain the parameters to positive values, we first took the square root of the parameters before entering the optimizer, and then squared them before use in calculating the predicted values used in the objective function. To minimize the objective function, MATLAB's built-in functions *fminsearch* and *lsqnonlin* were both implemented to test the stability of the direct-search (*fminsearch*) and gradient-based (*lsqnonlin*) minimizers. In each of the axial, circumferential, and simultaneous axial-circumferential parameter optimization protocols, the objective function (Equation 2.58) that was minimized was a normalized version of that by Ferruzzi *et al.* [10].

$$error = \sum_{i=1}^{n} \left[\left(\frac{(\Pi_z^{pred})_i - (\Pi_z^{ex})_i}{(\Pi_z^{ex})_i} \right)^2 + \left(\frac{(\Pi_\theta^{pred})_i - (\Pi_\theta^{ex})_i}{(\Pi_\theta^{ex})_i} \right)^2 \right] \qquad (2.58)$$

Here, *i* represents individual data points and *n* is the total number of data points while the superscripts *pred* and *ex* indicate stresses predicted by the model and calculated from the experimentally measured values, respectively.

Elastica Model

To further incorporate changes in the vascular microstructure, we also developed a modified elastica model in which fibers are assumed to be represented by the unbending of rods. Here, each collagen fiber was modeled individually and their contributions to the axial and circumferential directions were summed. Like the QLV model, axial and circumferential data were optimized individually. For this model, the value of elasticity was optimized to fit the experimental mechanical data using A nonlinear least-squares solver in MATLAB (*lsqnonlin*) with a minimum termination tolerance of 1e-5. The objective function minimized here was the same as that used for the fiber family models (Equation 2.58).

Summary of Parameter Estimations

Summaries of the parameter estimations used for each model are found in Tables 2.1-2.3.

Table 2.1: Parameter estimation for the QLV model. Here, the direct-search method *fminsearch* was used to determine the elastic moduli (E_z, E_θ), the relaxation time (b_1), the amplitude of relaxation time (C_1), and either the initial area (A_o) or initial length (L_o) of a vessel.

Model	$\varepsilon_j(t) = K(0)s_j^{(e)}[F_j(t)] + \int_{t_0}^t s_j^{(e)}[F_j(\gamma)]\frac{dK(t-\gamma)}{d\gamma}\,d\gamma$
Experimental	$\varepsilon_\theta = \frac{(1-\nu_{z\theta}\nu_{\theta z})}{E_\theta}\Pi_\theta \quad \varepsilon_z = \frac{(1-\nu_{\theta z}\nu_{z\theta})}{E_z}\Pi_z$
Objective Function	$\text{error} = \sqrt{\frac{\sum_{j=1}^n (X(t_j;w)-x_j)^2}{\sum_{j=1}^n x_j^2}}$
Parameters	$\phi_{circ} = \{A_o, E_\theta, C_1, b_1\} \; ; \; \phi_{ax} = \{L_o, E_z, C_1, b_1\}$

Table 2.2: Parameter estimation for the fiber family models. Here, both the direct-search *fminsearch* and gradient-based *lsqnonlin* methods were used to determine the stiffness of the isotropic contributions (c), stiffness of the anisotropic anisotropic ($c_1^1, c_1^2, c_1^{3,4}$), and non-dimensional anisotropic material parameters ($c_2^1, c_2^2, c_2^{3,4}$).

Model	$\Pi_i^{th} = c\left(\lambda_i^2 - \frac{1}{\lambda_i^2 \lambda_j^2}\right) + c_1^k(\lambda_i^2 - 1)exp[c_2^k(\lambda_i^2 - 1)^2]\lambda_i^2$
	$\quad + 2c_1^{3,4}(I_4^d - 1)exp[c_2^{3,4}(I_{4,i}^d - 1)^2]\lambda_i^2 \sin^2\alpha$
Experimental	$\Pi_\theta^{ex} = \frac{rp}{h} \quad \Pi_z^{ex} = \left(\frac{f}{2\pi\bar{r}h} + \frac{\bar{r}\bar{p}}{2h}\right)$
Objective Function	$error = \sum_{l=1}^n \left[\left(\frac{(\Pi_z^{th})_l - (\Pi_z^{ex})_l}{(\Pi_z^{ex})_l}\right)^2 + \left(\frac{(\Pi_\theta^{th})_l - (\Pi_\theta^{ex})_l}{(\Pi_\theta^{ex})_l}\right)^2\right]$
Parameters	$\phi = \{c, c_1^1, c_2^1, c_1^2, c_2^2, c_1^{3,4}, c_2^{3,4}\}$

Table 2.3: Parameter estimation for the Elastica Model. Here, j represents axial (z) or circumferential (θ) directions, E_θ is the elastic modulus of collagen fibers calculated using the circumferential data and E_z is the elastic modulus of collagen calculated using axial data.

Model	$\Pi_{j,tiss}^{th} = AF_{col,j}\Pi_j^f$
Experimental	$\Pi_\theta^{ex} = \frac{pr}{h} \quad \Pi_z^{ex} = \left(\frac{f}{2\pi rh} + \frac{pr}{2h}\right)$
Objective Function	$err_\theta = \sum_{i=1}^n \left(\frac{(\Pi_\theta^{th})_i - (\Pi_\theta^{ex})_i}{(\Pi_\theta^{ex})_i}\right)^2 \quad \sum_{i=1}^n \left(\frac{(\Pi_z^{th})_i - (\Pi_z^{ex})_i}{(\Pi_z^{ex})_i}\right)^2$
Parameters	$\phi_\theta = \{E_\theta\} \quad \phi_z = \{E_z\}$

2.7   Structural Quantification

Collagen fiber structures were quantified by tracing the collagen fibers imaged using second harmonic generation (SHG) with an Ultima Multiphoton Microscopy System (Prairie Technologies, Middleton, WI). Collagen is able to be imaged with SHG without staining because of it's non-symmetrical triple helix arrangement. Specifically, SHG takes place when the electric field from the exciting light deforms a non-symmetrical molecule and creates an oscillating field at twice the frequency (second harmonic) [23]. In our case, vessels were cannulated and placed in a custom-made system to place under the microscope were submerged in PBS and stretched to 40% of their *ex-vivo* length on a rod with a diameter matching that of the vessel to prevent the vessel from collapsing (Figure 2.11). To better match their inflated geometry, later vessels were also stretched on a cannula that closely matched the inner diameter of the vessel, stretched to 1.4 times the *ex-vivo* length, secured with small drops of glue at either end, and fixed with 10% formalin for up to 48 hours. Vessels were then transferred to 70% ethanol and transported to imaging under the multiphoton microscope where they were transferred to a custom-made device that held the vessels under PBS for imaging. After imaging was completed, vessels were transferred back to 70% ethanol. In each case, vessels were oriented such that the axial direction was aligned with the horizontal axis of the image and starting from the adventitia, a z-series of images across the vessel was was acquired with a 0.5 μm step size, 963 X 963 pixel field of view, and 2 μs dwell time with a 20X dipping objective at an excitation wavelength of 880 nm.

A custom written MATLAB code consisting of a combination of a gradient-based edge detection method via the derivative a Gaussian filter ('canny' option in MATLAB's *edge* function), filling of closed areas via the 'holes' option in MATLAB's *imfill*, turning fiber edges to traceable lines via 'thin' option of MATLAB's *bwmorph*, and removing noise using the 'clean' option of MATLAB's *bwmorph* which removed single white pixels surrounded by black pixels. Finally, intersecting areas (branch points) were removed and the end points were determined with the
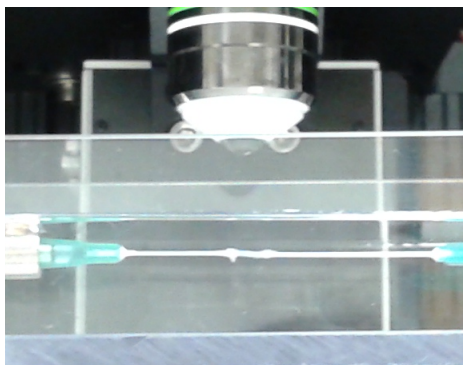
Figure 2.11: A vessel segment cannulated on each end submerged in PBS under a 20X dipping objective for MPM imaging.

Table 2.4: Measured tortuosities (T_o) and angles (α) for the fibers found in Figure 2.12. Note that fibers 1 and 2 are straight lines with tortuosity values of 1 and the correct angles of 90°and 0°, respectively.

Fiber Number	T_o	α [°]
1	1.00	90.00
2	1.00	0.00
3	10.85	-40.86
4	1.40	6.39
5	1.40	53.96

'branchpoints' option of *bwmorph* and *find*, respectively. The skeletonized fibers and their respective end points that resulted from this code were then used to determine the length and end-to end distance of each fiber. When determining the length of fibers, one end of the fiber was identified and tracing along the fiber, a value of 1 was added for white pixels adjacent to the current pixel and $\sqrt{2}$ for those located diagonally until the second end point was reached. This length and the distance between the two end points were then used in the calculation of tortuosity (Equation 2.45) and the angle from the horizontal to this end-to-end segment was used to determine the angle (Figure 3.5) of the fibers identified in the images. During the development of this code, a phantom image was analyzed to ensure fibers were properly traced (Figure 2.12). The same phantom image was also analyzed by hand using FIJI to validate the measurement of fiber length, angle, and tortuosity. Phantom values of tortuosity and fiber angle obtained can be found in Table 2.4.
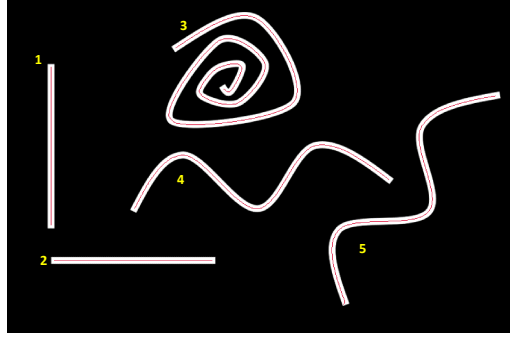
Figure 2.12: Phantom image overlaid with the skeletonized version of the fibers produced by custom code (red). The measured tortuosities (T_o) and angles (α) of fibers 1-5 are found in Table 2.4

After selecting one image that contained a full field of view of collagen, a secondary custom MATLAB code was used to create images of the side views of the stack. The new image was filtered and binarized so that the white pixels (collagen) could easily be summed (Figure 2.13) and represented by the area in the cross-sectional view of the image (A_{fibers}). The pixels corresponding to the 5 images nearest the one of interest were also counted (A_{image}) so as to calculate the area fraction of collagen (Equation 2.59) represented by the image of interest. This value was then used to scale the computed stress up from the sum of those determined from the fibers in the image chosen up to the collagen imaged across the vessel thickness. Finally, images of collagen were opened in Fiji where the approximate fiber diameter was measured by hand using the straight line tool and measuring the calibrated length of the line drawn. The length was calibrated with the calibration tool by specifying the size of the pixels as output from the MPM system (0.317 x 0.317 μm).

$$AF_{col} = \frac{A_{fibers}}{A_{image}} \tag{2.59}$$

39
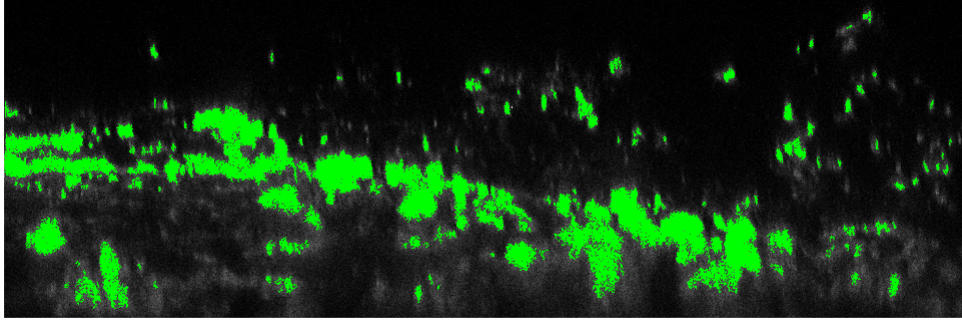
Figure 2.13: Collagen identified (Green) in the x-z plane of a stack of MPM images through the vessel thickness of a week 4 MCT LPA.

2.7.1 Data Collected

For each animal, data were collected for each the left and right pulmonary artery. For each artery, axial and circumferential mechanical data and MPM images were collected. In the axial mechanics, constant flow was prescribed that corresponded with a constant pressure matching the measured *in vivo* mPAP. This constant pressure resulted in an approximately constant circumferential stretch. While the vessel was constantly pressurized, the axial length was cyclically changed resulting in varying axial stretch (between 1.4 and 1.45) and therefore stress. During the circumferential mechanical test, constant axial stretch, cyclical flow causing cyclical variations in diameter resulting in cyclical circumferential stretch and stress were collected. Along with mechanical data, multiphoton images of collagen were collected and used for microstructural measurements. Such microstructural information include tortuosity, fiber angle, and collagen fraction.

3 Results

Male Sprague-Dawley rats were injected with monocrotaline to induce PAH. While all of the earlier week animals survived to their date of experiments, not all late stage disease animals survived to their surgery date. Of the animals that did survive, vessels were imaged via MPM and vascular mechanics were tested in a tubular biaxial system and modeled with constitutive models. Herein, we present the results of these experiments.

3.1 Hemodynamic Data

Of 64 animals that were injected with MCT, 23 were designated as week four (late stage disease). Of these animals, 52% (22 animals) survived to the date of experiments. No other animals died prematurely. On the date of experiments, blood pressure measurements in the right ventricle and pulmonary arteries (Figure 3.1) were first taken to confirm the health state of the animals. Mean pulmonary arterial pressure for control animals was 20.46±4.25 and 45.79±5.64 mmHg for advanced state PAH animals.

3.2 Mechanical Data

Using values measured *in vivo*, vessels were mechanically tested at cyclical pressure with constant axial length (circumferential protocol) and cyclical axial stretch at constant mPAP (axial protocol). The pressure, diameter, and axial load and length were all first collected as a time series
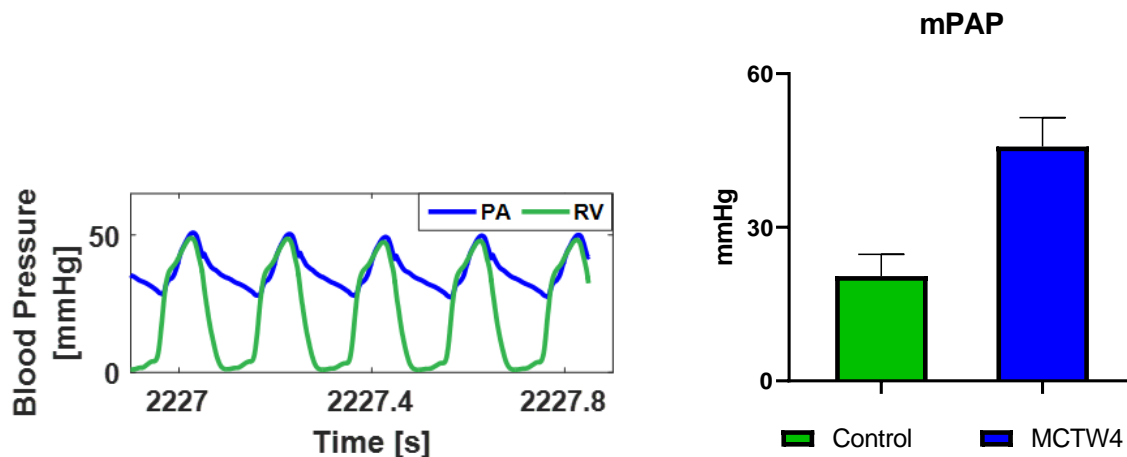
Figure 3.1: Left: Blood pressure measurements over time in the main pulmonary artery (blue) and right ventricle (green). Right: mean pulmonary arterial pressure in control (green) and hypertensive (blue) animals.

(Figures 2.6-2.7) and later converted to stress-strain loops. These tests were ran twice to confirm mechanical reproducibility and stability. Examples of reproducible data chosen for analysis can be found in Figure 3.2 and examples of resulting stress-strain loops are outlined in Figures 3.3-3.4. In these results, the hysteresis was much larger in the axial protocol than in the circumferential. Therefore, four cycles in which diameter, pressure, and load were consistent were chosen for QLV modeling to investigate the stiffness and time-dependent properties of the tissues. Later, one unloading phase was used to train our microstructural model since the unloading phase reflects the energy stored *in vivo* [11].

3.2.1 Structural/Multiphoton Microscopy

Collagen fibers were imaged in a z-series starting from the adventitia and continued toward the intima until the fibers could no longer be identified via multiphoton microscopy. This resulted in stacks of images ranging between 180 and 300 images. While the fibers were highly tortuous and randomly oriented in control arteries, they became engaged and tended to a preferred direction in the diseased state (Figures 3.5-3.6).
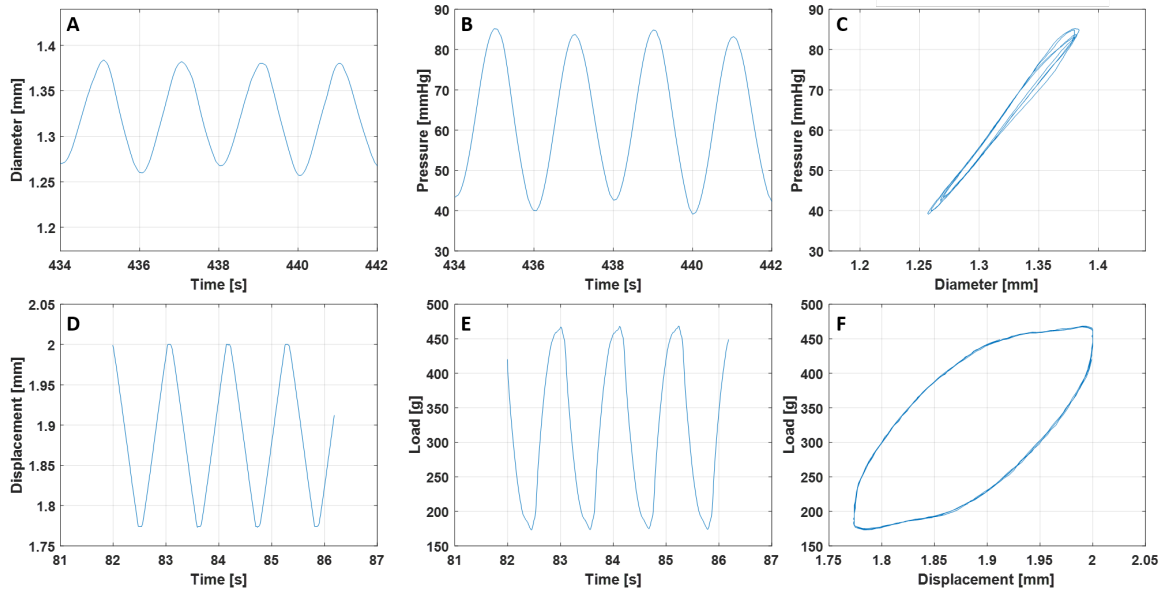
Figure 3.2: Measured data from the tubular biaxial protocols. In the circumferential protocol (top row), diameter (A) and pressure (B) are measured to produce diameter-pressure loops (C). In the axial protocol, axial displacement (D) and load (E) are measured to produce axial displacement-load loops (F).

3.3 Model Fitting and Model Parameters

3.3.1 Quasi-linear Viscoelasticity

Due to the nature of the mechanical testing (separate axial and circumferential protocols), the two mechanical axes were analyzed individually with QLV models. The two models used predicted cross-sectional area (circumferential mechanics) as a function of time and vessel lengthening as a function of axial load (axial mechanics). Each of these models characterized mechanical properties via optimization of parameter values initially set to values from literature [57]. A summary of the optimal values for the axial and circumferential directions can be found in Tables 3.2 and 3.2, respectively [44].

In the circumferential direction, the modulus of elasticity and the relaxation time significantly changed from control to week 4 MCT. Specifically, the modulus of elasticity (E_θ) significantly increased from the control and week one of MCT to week four of MCT. When the

Table 3.1: Summary of the optimized parameters from the QLV model of left and right pulmonary arteries in the circumferential protocol. N is the number of vessels in the group, $\hat{A}_o$ is the reference cross-sectional area of the vessel, E_θ is the modulus of elasticity, and $C_{1,\theta}$ is the amplitude associated with the relaxation time ($b_{1,\theta}$). $J(\phi)$ is the normalized root-mean square error and R^2 is the coefficient of determination.

		N	$E_\theta \times 10^3$ (mmHg)	$C_{1,\theta} \times 10^{-2}$	$b_{1,\theta} \times 10^{-4}$ (sec)	$J(\phi) \times 10^{-4}$	R^2
PL	LPA	4	1.88 ± 1.62	51.8 ± 1	5.16 ± 0.03	0.64 ± 0.27	0.968 ± 0.012
	RPA	5	3.42 ± 3.1	52.1 ± 1.7	5.05 ± 0.05	0.28 ± 0.1	0.969 ± 0.019
MCTW1	LPA	5	2.31 ± 1.24	52.6 ± 1.4	5.1 ± 0.05	0.71 ± 0.25	0.994 ± 0.002
	RPA	5	1.42 ± 0.73	52.2 ± 0.08	5.2 ± 0.007	0.75 ± 0.14	0.983 ± 0.006
MCTW4	LPA	5	7.62 ± 2.81	52.4 ± 1.3	5.08 ± 0.05	0.64 ± 0.1	0.976 ± 0.011
	RPA	5	22.88 ± 12.68	51.9 ± 1.1	5.1 ± 0.03	0.34 ± 0.2	0.99 ± 0.004

Table 3.2: Summary of the optimized parameters from the QLV model of left and right pulmonary arteries in the axial protocol. N is the number of vessels in the group, $\hat{L}_o$ is the reference length of the vessel, E_z is the axial modulus of elasticity, and $C_{1,z}$ is the amplitude associated with the relaxation time ($b_{1,z}$). $J(\phi)$ is the normalized root-mean square error, and R^2 is the coefficient of determination.

		N	$E_z \times 10^6$ (mmHg)	$C_{1,z}$	$b_{1,z}$ (sec)	$J(W) \times 10^{-4}$	R^2
PL	LPA	4	3.28 ± 0.82	0.83 ± 0.34	0.12 ± 0.02	6.72 ± 1.08	0.994 ± 0.002
	RPA	6	3.48 ± 2.22	0.89 ± 0.28	0.15 ± 0.06	7.86 ± 1.16	0.993 ± 0.002
MCTW1	LPA	3	1.29 ± 0.60	1.00 ± 0.00	0.18 ± 0.01	11.8 ± 0.99	0.986 ± 0.003
	RPA	3	1.31 ± 0.63	1.00 ± 0.00	0.23 ± 0.02	13.8 ± 3.19	0.979 ± 0.011
MCTW4	LPA	6	2.25 ± 0.52	0.98 ± 0.06	0.13 ± 0.03	7.48 ± 1.39	0.993 ± 0.003
	RPA	7	3.45 ± 1.54	0.89 ± 0.13	0.13 ± 0.03	6.90 ± 1.03	0.994 ± 0.002
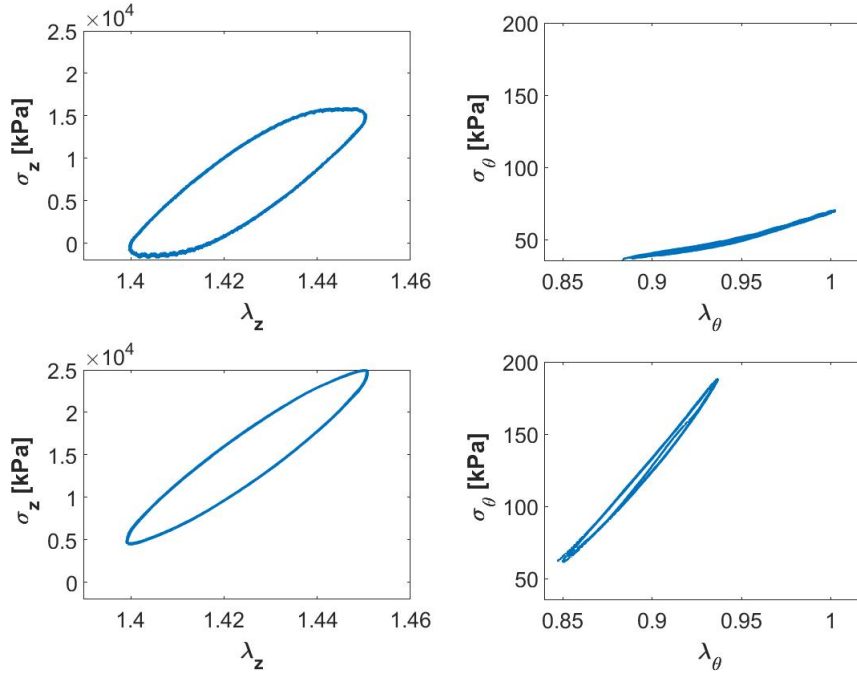
Figure 3.3: Example mechanics of the left pulmonary artery from normotensive (top panels) and hypertensive (bottom panels) animals in the axial (left panels) and circumferential (right panels) directions. Note that axial stress is two orders of magnitude greater than circumferential. Note that the unit of axial stress is megapascals whereas the unit of circumferential stress is kilopascals.

relaxation time was transformed through the natural log of the parameter, it became significantly larger in the RPA of MCT week 1 compared to that of the placebo. Axially, the modulus of elasticity decreased from the placebo to early stage disease (MCTW1), but increased in the late stage to values similar to placebo. The opposite trend was seen in the relaxation time of the axial direction, meaning vessels become softer and increase buffering abilities at early stage disease, but recover these properties at late stage disease [44]. Additionally, the relaxation time was much greater in the axial direction than the circumferential but did not change significantly with disease progression in either left or right pulmonary arteries.
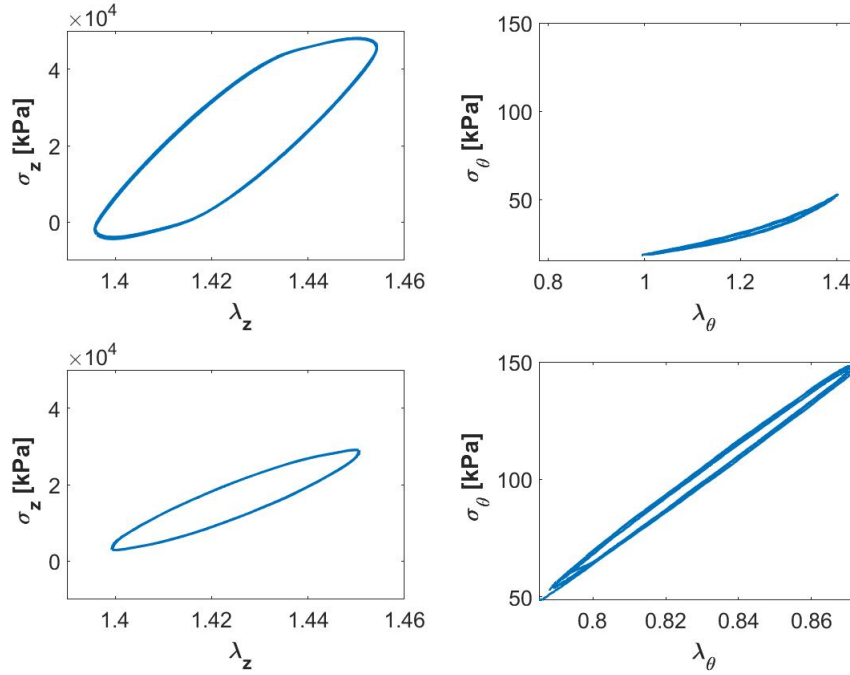
Figure 3.4: Example mechanics of the right pulmonary artery from normotensive (top panels) and hypertensive (bottom panels) animals in the axial (left panels) and circumferential (right panels) directions. Note that axial stress is two orders of magnitude greater than the circumferential direction.

3.3.2 Fiber Family Models

For each of the fiber family models, uniaxial data was first fit by optimizing an initial guess. The resulting parameters were then re-entered as an initial guess to assess the stability of the optimal parameter sets. If the resulting parameters from the second optimization did not differ from the guess, the solution was deemed stable.

While the one-fiber family model was able to predict the axial and circumferential data individually, it failed to predict the two combined. Here, the difference in magnitude of the two data sets was too great for the shared parameters to fit simultaneously. Similarly, the two-fiber family model was able to predict the individual axial and circumferential data. Although it was also able to predict the two simultaneously, the optimal parameter sets varied greatly between vessels. Additionally, this model did not provide nor was it informed by changes in collagen organization.
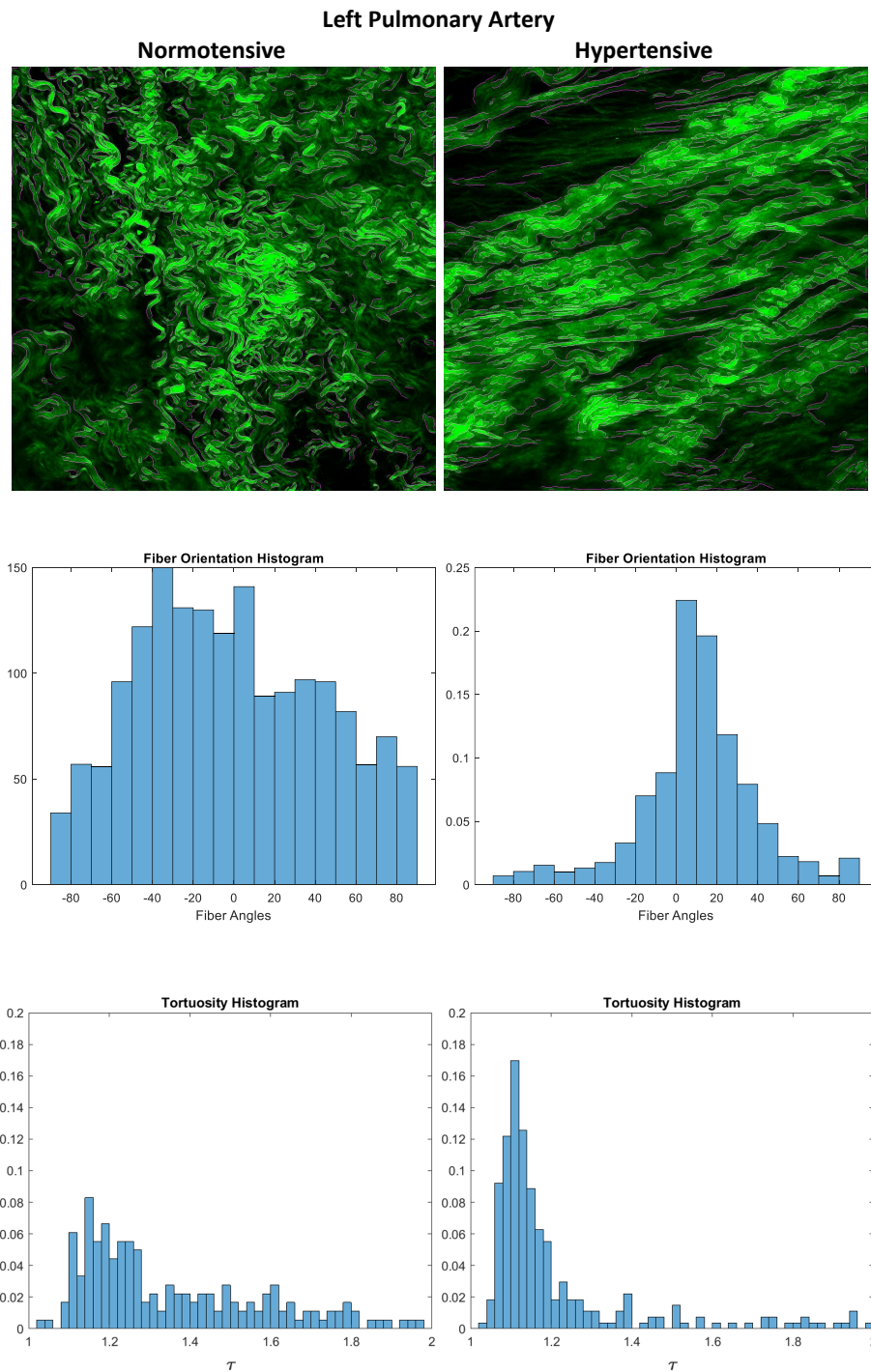
Figure 3.5: Example multiphoton images (top) from the LPA of a normotensive (left) and hypertensive (right) animal with their respective distributions of fiber orientations (middle) and tortuosities (bottom). Note that the fibers become straighter and more aligned in the hypertensive state.
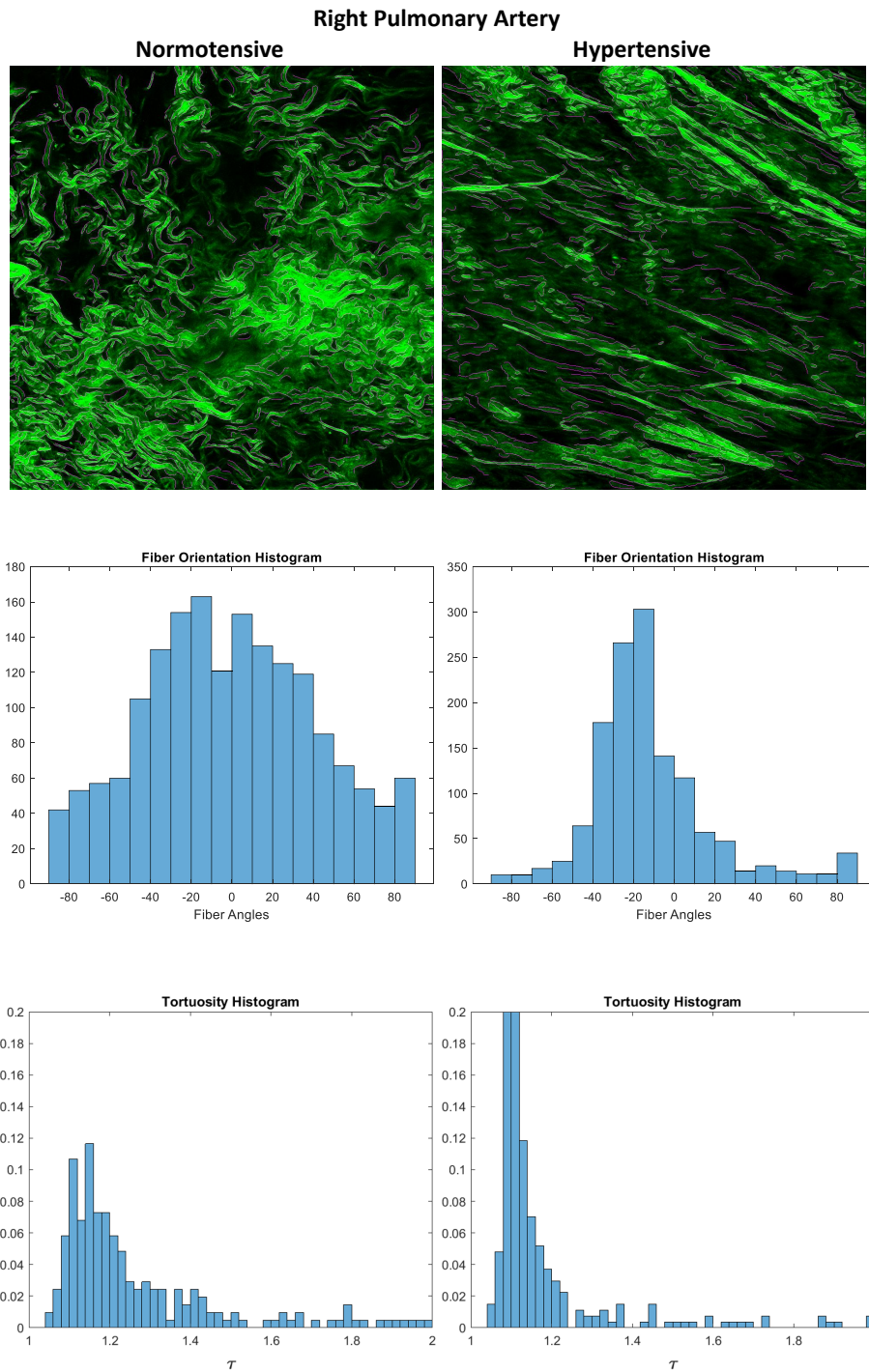
Figure 3.6: Example multiphoton images (top) from the RPA of a normotensive (left) and hypertensive (right) animal with their respective distributions of fiber orientations (middle) and tortuosity (bottom).Note that fibers become straighter and more aligned in the hypertensive state.

**Table 3.3**: Parameter results from one-fiber family modeling of right pulmonary arteries in advanced disease. Note that the error was very high for each sample (1-2 orders of magnitude higher than other models), indicating that the model was not able to fit well the axial and circumferential data simultaneously.

	c [MPa]	c1 [MPa]	c2	error
Sample 1	6.9	6.1e4	-10.7	73.1
Sample 2	-2.7	3.11e13	-36.6	61.4
Sample 3	2.47	2.59e20	-56.9	51.0

Table 3.4: Parameter results from two-fiber family modeling of right pulmonary arteries in advanced disease.

	c [kPa]	C_1^1 [kPa]	C_2^1	C_1^2 [kPa]	C_2^2	error
Sample 1	2.5e-7	37.7	6.8	580.1	5.6	0.4
Sample 2	814.7	17.1	7.4	1.4e+3	-20	2.2
Sample 3	6.3e+3	2.6	8.9	-2.24e+3	7.3	1.1
Sample 4	6.8e-6	38.8	6.7	-1.9e+3	-15	0.6

Four-fiber Family Model

Initial efforts to fit this model allowed the parameters to reach negative values. Here, the model was able to predict many of the data sets. However, the parameters represent material properties such as stiffness. Therefore, the parameters were then constrained to positive values. Once constrained, the model no longer predicted half of the data sets. Because the direct-search method (*fminsearch*) tends to be more sensitive to changes in initial guesses, we also implemented a non-linear, gradient-based optimization method (*lsqnonlin*). Although trials indicated that *lsqnonlin* was less sensitive to changes in our initial guess and was able to fit the individual axial and circumferential data well, it was still unable to fit the model to half of our biaxial data. For some of the vessels, the model was not able to reach the correct concavity. To address this, the exponents in the model were allowed to reach negative values since they are not related to stiffness and are unitless. While allowing negative exponential values resulted in better circumferential fittings, the simultaneous fittings did not improve over the constrained parameter fittings. Regardless of the modeling effort, there was not a trend in parameter values (summary of

Table 3.5: Summary of Optimized parameters from the Four-fiber Family model of right pulmonary arteries from five control and four late-stage disease animals. While parameter representing stiffness in the circumferential direction (C_1^2) did increase, changes in parameters were not significant.

		C [kPa]	C_1^1 [MPa]	C_2^1	C_1^2 [kPa]	C_2^2	$C_1^{3,4}$ [kPa]	$C_2^{3,4}$	error
CTL	Average	68.6	-1.41e2	4.63	-1.19e5	8.94	3.60e4	7.5	0.93
	STDEV	106.8	2.14e2	7.14	2.67e5	23.49	8.01e4	7.16	1.49
MCTW4	Average	191.7	-0.51	-1432.61	-8.60e3	3.24	1.23	10.68	0.27
	STDEV	217.8	1.02	2885.98	1.72e4	36.69	2.27	6.20	0.26

optimized parameters in Table 3.5). Therefore, we also attempted a model that incorporated the microstructural properties of individual fibers.

3.3.3   Elastica Model

To ensure proper building of the Elastica Model, we reproduced results from previously reported papers (Figure 3.7). Specifically, we reproduced the calculations of θ_o for varying stretch values as reported by MacKenna et al. [34] and θ_1 by Ling and Chow for any measured fiber fiber tortuosity [32]. We were then able to transform fiber tension calculated in the model to their contributions to tissue mechanics, summed over all of the fibers measured, and scaled up to the full thickness of the tissue.

Because this model only included the optimization of a single parameter, it was much less sensitive to initial guesses entering the optimizer. To date, the mechanics were optimized separately as was done with the QLV model.
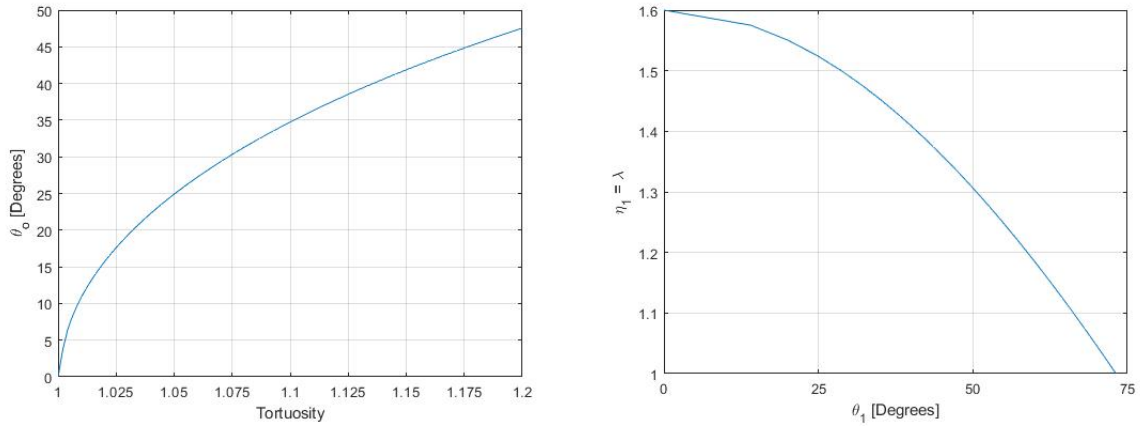
Figure 3.7: Here, we were able to successfully predict θ_o for multiple tortuosity values (right) and θ_1 for multiple values of fiber stretch (right).
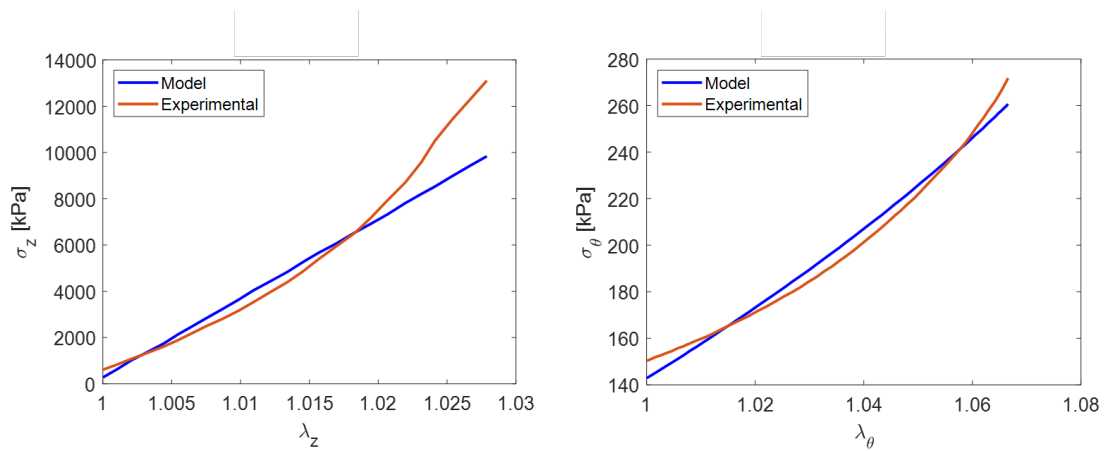
Figure 3.8: Examples of elastica model (blue) fittings of axial (left) and circumferential (right) experimental data (orange). Note that the stress levels are different between axes.

4 Discussion

4.1 Mechanical and Microstructural Properties

Pulmonary arteries were tested in a tubular biaxial system which demonstrated higher hysteresis effects in the axial direction than the circumferential direction. Therefore, to better characterize the mechanical differences in the two directions and between vessels of animals at different stages of disease, we implemented the QLV model. Our results revealed that the relaxation time in the axial direction was greater in axial direction than in the circumferential direction, but did not change with disease progression. Furthermore, the elastic modulus in the circumferential direction increased further in the right pulmonary artery than left at late stage disease. Furthermore, fibers became less tortuous and aligned in a preferred direction with disease progression. However, the fibers were analyzed near the center of the vessel wall and became aligned in the axial direction which was not the direction of increased stiffness. However, this may be remedied by analysis of fiber diameter as well as analysis of fibers throughout the vascular wall since the orientation of fibers in the aorta vary depending on vessel wall layer [47]. Furthermore, future studies should determine the best method of analysing the statistical differences in histograms of fiber angles and tortuosities since the distributions may not be considered normal.

4.2   Model Findings

While the QLV models were able to provide mechanical and time-dependent information on the vessels, they were not able to explain the reason behind changes during disease progression. Therefore, we explored several microstructural models. The first of which was the one-fiber family model in which constituents of the vessel are assumed to belong to the same orientation with the tissue. This model, however, had too few parameters to predict the mechanical behavior of vessels in both the axial and circumferential directions. Therefore, the two-fiber family model was implemented. In this model, vessel wall constituents were assumed to belong in either the axial or the circumferential direction. Any other directions would then be broken down to their projections or contributions to these directions. While this model provided more parameters to better fit measured mechanics, it was not able to fit the two directions simultaneously and neglects the importance of fibers that do not belong in the axial or circumferentially oriented categories. Hence, the four-fiber family model was explored in an attempt to include contributions from the axial, circumferential, and two symmetrically oriented fiber groups. This model was able to fit both axial and circumferential data simultaneous. However, finding a unique solution proved difficult due to the overparameterization of the model.

We also explored the use of the Elastica Model which assumes quarter periods of sinusoidal collagen to be modeled as bent rods in their unloaded state and attributes tissue mechanics to the unbending of these rods. However, to date, important fiber morphologies such as individual fiber diameters have yet to be determined and the implementation of simultaneously modeling axial and circumferential mechanics.

4.3   Limitations

One limitation to this study was the animal model used. While the monocrotaline is a well established model of PAH, it also has some drawbacks. For instance, the monocrotaline model is

associated with high mortality past 3 weeks of injection and earlier impacts on the right ventricle compared to other models [21]. Therefore, our numbers of week 4 MCT animals were relatively low. These sudden deaths appear to be related to the toxicity of crotaline which does not solely affect the lungs [58].

In the current configuration, the Elastica model works under the assumption that all collagen fibers have the same diameter and stiffness. The stiffness may not, and the diameters certainly are not equal for all collagen fibers in pulmonary arteries. Furthermore, this model currently works under the assumption that all fibers have the same periodicity - which is not the case and should be addressed in future studies. Another limitation to the current Elastica Model is that it does not account for straight fibers ($T_o = 1$). In other words, once a fiber is unbent, the stress it experiences becomes infinitely great and can cause problems when trying to model tissue which was stretched beyond what should be possible for the fibers to stretch. In these cases, it is possible that the fiber rotates to accommodate further stretch in a given direction, though this would need to be added to the model and explored in mechanical tests under microscopy. Furthermore, fibers were imaged at unequal stretch ($\lambda_z = 1.4$ and $\lambda_\theta \approx 1$). This may affect the results of modeling efforts because as tissues are stretched, they become more engaged and realign in the direction of greater load [4]. While efforts were taken to reverse the unequal stretching of the tissue when imaging, these efforts were made under the assumption that the stretching of the tissue is directly translated to the stretching of the fibers and not affected by other constituents of the vessel such as smooth muscle cells or elastin. The elastica model also struggled to fit axial data at *in vivo* stretch values. This is likely due to the shape of the curve - the elastica model does not account for a large "toe region" in a stress-stretch curve. Therefore, adding other terms to the model which represent the toe region (such as elastin contributions) or testing tissues at lower stretch values may improve modeling efforts. Lastly, the elastica model was not able to predict circumferential stress at tissue stretch levels much greater than or less than one. This could be due to the fact that the model does not account for compression of fibers and is not defined at

stretch values greater than the fiber tortuosity.

4.4 Future Studies

4.4.1 Animal Model

While the current study attempts to better understand progression of pulmonary arterial hypertension, future studies can improve upon the attempts of inducing PAH. For instance, another model of PAH, called the sugen-hypoxia (SuHx) model is induced via a double-hit with sugen and hypoxia. Here, animals are injected with a dose of SU5416 and then kept in a hypoxic environment (10% oxygen) for three weeks and then returned to normoxia to allow PAH to reach a severe state which mimics more closely symptoms found in human lungs such as plexiform lesions [1, 39, 52]. This animal model is also less susceptible to sudden death. Additionally, our methods included the use of male Sprague-Dawley rats due to the reproducibility of male rats as a result of their hormones fluctuating less than females. However, PAH is a disease that affects women 2-4 times more often than men than men [12, 16, 31]. Females also tend to tolerate PAH better as indicated by increased survival rates compared to males [12]. Therefore, future studies should include the use of female rats.

4.4.2 Image Analysis

More detailed image analysis should also be implemented in future studies. Currently, we assume that each fiber has the same periodicity. However, initial inspection of MPM images indicates this is not the case. Therefore, a code that determines the periodicity of each individual fiber should be developed. One method of determining periodicity is determining how many times a fiber intersects with its mid-line (straight end-to-end path). Another method to investigate would be measuring the distance between the peaks of each individual fiber. We also currently assume

all fibers share the same diameter which was determined by taking the average of sampled fibers measured in FIJI. However, the resolution of current fiber images allows for the edge detection of one side of a fiber, but loses the other edge of the fiber. One promising solution is neural network techniques which recognize objects of interest and enhances them. Should this work, we could better determine the diameter of the fibers either with a code that calculates the area and length of fibers and calculates the diameter by assuming the fiber image would straighten out into a rectangle, or moves perpendicular from one edge and counts the distance it moves until it reaches the other edge of the fiber.

4.4.3   Arterial Mechanics

Although the difference stress levels between the axial and circumferential direction is large, we would like to model the two directions simultaneously since the same fibers with one stiffness are contributing to each. To do this, experiments may need to be conducted at lower ranges of pressure and stretch so that the axial and circumferential stress levels can more easily be matched. Furthermore, our study determined that the left and right pulmonary arteries remodel asymmetrically. To determine a more specific initial remodeling location, future studies may investigate proximal and distal segments of these vessels.

4.4.4   Modeling Efforts

While the elastica model incorporates several collagen structural properties and weights fiber contributions to tissue mechanics via image analysis, it is possible that the microscopy efforts do not reveal all collagen in the tissue or the amount of collagen changing with disease progression. To account for such changes, a scaling term representing the total collagen content may be added. Such a value can be determined through a hydroxyproline assay. Additionally, we recognize that there are other microstructural elements that we are not considering. Therefore,

future studies may include model components representing elements such as collagen cross-linking [53] or elastin [29, 63, 64]. For these models, additional parameters associated with cross-linking and elastin may be added to the list of optimized values. If this adds too many additional parameters, elastin can be imaged with a multiphoton microscope via autofluorescence in a similar manner as SHG was used to image collage.

4.4.5 Imaging

Finally, future works may involve the use of autofluorescence to image and validate the parameters associated with elastin. Future studies can image elastin via two photon excited fluorescence and collagen via SHG simultaneously with an excitation wavelength of 800-810 nm and the appropriate bandpass filters for elastin and collagen [4, 50, 63, 64].

Bibliography

[1] ABE K., TOBA M., ALZOUBI A., ITO M., FAGAN K.A., COOL C.D., VOELKEL N.F., MCMURTRY I.F., AND OKA M. *Formation of Plexiform Lesions in Experimental Severe Pulmonary Arterial Hypertension* Circulation, Vol.121 pp. 2747-2754, 2010.

[2] BERTERO T., COTTRILL K.A., YU L., HAEGER C.M., DIEFFENBACH P., ANNIS S., HALE A., BHAT B., KAIMAL V., ZHANG Y., GRAHAM B.B., KUMAR R., SAGGAR R., SAGGAR R., WALLACE W.D., ROSS D.J., BLACK S.M., FRATZ S., FINEMAN J.R., VARGAS S.O., HALEY K.J., WAXMAN A.B., CHAU B.N., FREDENBURGH L.E., AND CHAN S.Y. *Matrix Remodeling Promotes Pulmonary Hypertension through Feedback Mechanoactivation of the YAP/TAZ-miR-130/301 Circuit* Cell Reports, Vol.13 pp. 1016-1032, 2015.

[3] BUDAS G.R., BOEHM M., KOJONAZAROV B., VISWANATHAN G., TIAN X., VEEROJU S., NOVOYATLEVA T., GRIMMINGER F., HINOJOSA-KIRSCHENBAUM F., GHOFRANI H.A., WEISSMANN N., SEEGER W., LILES J.T., AND SCHERMULY R.T. *ASK1 Inhibition halts Disease Progression in Preclinical Models of Pulmonary Arterial Hypertension* Am. J. Respir. Crit. Care Med., Vol.197(3) pp. 373-385, 2017.

[4] CHOW M., TURCOTTE R., LIN C.P., AND ZHANG Y. *Arterial Extracellular Matrix: A Mechanobiological Study of the Contributions and Interactions of Elastin and Collagen* Biophysical Journal, Vol.106 pp. 2684-2692, 2014.

[5] DEBES J. AND FUNG Y.C. *Biaxial Mechanics of Excised Canine Pulmonary Arteries* Am J. Physiol., Vol.269(2 Pt 2) pp. H433-H442, 1995.

[6] DREXLER E.S., QUINN T.P., SLIFKA A.J., McCOWAN C.N., BISCHOFF J.E., WRIGHT J.E., IVY D.D., AND SHANDAS R. *Comparison of Mechanical Behavior Among the Extrapulmonary Arteries from Rats* Journal of Biomechanics, Vol.20 pp.812-819, 2007.

[7] DREXLER E.S., BISCHOFF J.E., SLIFKA A.J., McCOWAN C.N., QUINN T.P., SHANDAS R., IVY D.D., AND STENMARK K.R. *Stiffening of the Extrapulmonary Arteries From Rats in Chronic Hypoxic Pulmonary Hypertension* Journal of Research of the National Institute of Standards and Technology, Vol.113 pp. 239-249, 2008.

[8] ELLIS R., LEIGH R., SOUTHAM D., O'BYRNE P.M., AND INMAN M.D. *Morphometric Analysis of Mouse Airways after Chronic Allergen Challenge* Lab. Investig., Vol.83(9) pp. 1285-1291, 2003.

[9] FERRUZZI J, VORP DA, AND HUMPHREY JD. *On Constitutive Descriptors of the Biaxial Mechanical Behaviour of Human Abdominal Aorta and Aneurysms.* J. R. Soc. Interface, Vol. 8, pp. 435-450, July 2010.

[10] FERRUZZI J., COLLINS M.J., YEH A.T., AND HUMPREY J.D. *Mechanical Assessment of Elastin Integrity in Fibrillin-1-deficient Carotid Arteries: Implications for Marfan syndrome* Cardiovascular Research (European Society of Cardiology), Vol.92 pp. 287-295, 2011.

[11] FERRUZZI J., BERSI M.R., AND HUMPHREY J.D. *Biomechanical Phenotyping of Central Arteries in Health and Disease: Advantages of and Methods for Murine Models* Annals of Biomedical Engineering, Vol.41 pp. 1311-1330, 2013.

[12] FODERARO A. AND VENTETUOLO C.E *Pulmonary Arterial Hypertension and the Sex Hormone Paradox* Curr Hypertens Rep, Vol18(84) pp. 1-8, 2016.

[13] FREED A.D. AND DOEHRING T.C. *Elastic Model for Crimped Collagen Fibrils* J. Biomech. Engr., Vol.127(4) pp. 587-593, 2005.

[14] FUNG Y.C. *A First Course in Continuum Mechanics: Third Edition* Prentice Hall, Englewood Cliffs, NJ, 1994.

[15] FUNG Y.C. *Biomechanics: Circulation* Springer-Verlag, New York, 1997.

[16] GAINE S.P. AND RUBIN L.J. *Primary Pulmonary Hypertension* The Lancet Vol.352(9129) pp. 719-725, 1998

[17] GASSER T.C., OGDEN R.W., AND HOLZAPFEL G.A. *Hyperelastic Modelling of Arterial Layers With Distributed Collagen Fibre Orientations* Journal of the Royal Society Interface, Vol.3 pp. 15-35, 2005.

[18] GASSER T.C., GALLINETTI S., XING X., FORSELL C., SWEDENBORG J., AND ROY J. *Spatial Orientation of Collagen Fibers in the Abdominal Aortic Aneurysm's Wall and its Relation to Wall Mechanics* Acta Biomaterialia, Vol.352 pp. 719-725, 2012.

[19] GASSER T.C. *Aorta* Biomechanics of Living Organs, pp 169-191, 2017.

[20] GERRINGER J.W., WAGNER J.C., VELEZ-RENDON D., AND VALDEZ-JASSO D. *Lumped-parameter Models of the Pulmonary Vasculature During the Progression of Pulmonary Arterial Hypertension* Physiol. Rep., Vol.6(3) pp. e13586 1-12, 2018.

[21] GOMEZ-ARROYO J.G., FARKAS L., ALHUSSAINI A.A., FARKAS D., KRASKAUSKAS D., VOELKEL N., AND BOGAARD H.J. *The Monocrotaline Model of Pulmonary Hypertension in Perspective* Am. J. Physiol. Lung Cell Mol. Physiol., Vol.302 pp. L363-L369, 2012.

[22] GORFIEN S.F., HOWARD P.S., MYERS J.C., AND MACARAK E.J. *Cyclic Biaxial Strain of Pulmonary Artery Endothelial Cells Causes an Increase in Cell Layer-associated Fibronectin* Am. J. Respir. Cell Mol. Biol., Vol.3 pp. 421-429, 1990.

[23] HILL M.R., DUAN X., GIBSON G.A., WAtkins S., AND ROBERSON A.M. *A Theoretical and Non-destructive Experimental Approach for Direct Inclusion of Measured Collagen Orientation and Recruitment Into Mechanical Models of the Artery Wall* Journal of Biomechanics, Vol.45 pp. 762-771, 2011.

[24] HOLZAPFEL G.A., GASSER T.C, AND OGDEN R.W. *A New Constitutive Framework for Arterial Wall Mechanics and a Comparative Study of Material Models* Journal of Elasticity, Vol.61 pp. 1-48, 2000.

[25] HOLZAPFEL G.A. *Nonlinear Solid Mechanics: A Continuum Approach for Engineering* Wiley, West Sussex, England, 2010.

[26] HUANG W., DELGADO-WEST D., WU J.T., AND FUNG Y.C. *Tissue Remodeling of Rat Pulmonary Artery in Hypoxic Breathing. II. Course of Change of Mechanical Properties* Annals of Biomedical Engineering, Vol.29 pp. 552-562, 2001.

[27] HUMPHREY J.D., DELANGE S.L. *An Introduction to Biomechanics: Solids and Fluids, Analysis and Design* Springer, New York, N.Y., 2004.

[28] HUMPHREY J.D., EBERTH J.F., DYE W.W., AND GLEASON R.L. *Fundamental Role of Axial Stress in Compensatory Adaptations by Arteries* Journal of Biomechanics, Vol.42 pp. 1-8, 2009.

[29] KAO P.H., LAMMERS S.R., TIAN L., HUNTER K., STENMARK K.R., SHANDAS R., AND QI H.J. *A Microstructurally Driven Model for Pulmonary Artery Tissue* J. Biomech. Eng., Vol.133(5) pp. 051002, 2011.

[30] KOBS R.W., MUVARAK N.E., EICKHOFF J.C., AND CHESLER N.C. *Linked Mechanical and Biological Aspects of Remodeling in Mouse Pulmonary Arteries with Hypoxia-induced Hypertension* Am J Physiol Heart Circ Physiol, Vol.288 pp. H1209-H1217, 2005.

[31] LAI Y.C., POTOKA K.C., CHAMPION H.C., MORA A.L., AND GLADWIN M.T. *Pulmonary Arterial Hypertension: The Clinical Syndrome* Circulation Research, Vol.115 pp. 115-130, 2013.

[32] LING S.C. AND CHOW C.H. *The Mechanics of Corrugated Collagen Fibrils in Arteries* J. Biomechanics, Vol.10 pp. 71-77, 1977.

[33] LIU F., HAEGER C.M., DIEFFENBACK P.B., SICARD D., CHROBAK I., CORONATA A.M.F., SUAREZ VELANDIA M.M., VITALI S., COLAS R.A., NORRIS P.C., MARINKOVIC A., LIU X., MA J., ROSE C.D., LEE S, COMHAIR S.A.A., ERZURUM S.C., MCDONALD J.D., SERHAN C.N., WALSH S.R., TSCHUMPERLIN D.J., AND

FREDENBURGH L.E. *Distal Vessel Stiffening is an Early and Pivotal Mechanobiological Regulator of Vascular Remodeling and Pulmonary Hypertension* JCI Insight, Vol.1(8) pp. 1-20, 2016.

[34] MACKENNA D.A. *Contribution of the Extracellular Collagen Matrix to the Mechanics of Ventricular Myocardium (PhD thesis)* University of California, San Diego, 1994.

[35] MACKENNA D.A., OMENS J.H., AND COVELL J.W. *Left Ventricular Perimysial Collagen Fibers Uncoil Rather Than Stretch During Diastolic Filling* Basic Research in Cardiology, Vol.91(2) pp. 111-122, 1996.

[36] MACKENNA D.A., VAPLON S.M., AND MCCULLOCH A.D *Microstructural Model of Perimysial Collagen Fibers for Resting Myocardial Mechanics During Ventricular Filling* Modeling in Physiology, pp. H1576-H1586, 1997.

[37] MAARMAN G., LECOUR S., BUTROUS G., THIENEMANN F., AND SLIWA K. *A Comprehensive Review: The Evolution of Animal Models in Pulmonary Hypertension Research; Are We There Yet?* Pulm. Circ., Vol.3(4) pp. 739-756, 2013.

[38] MONSON K.L., BARBARO N.M.,AND MANLEY G.T. *Biaxial Response of Passive Human Cerebral Arteries* Annals of Biomedical Engineering, Vol.36(12) pp. 2028-2041, 2008.

[39] NICOLLS M.R., MIZUNO S., TARASEVICIENE-STEWART L., FARKAS L., DRAKE J.I., AL HUSSEINI A., GOMEZ-ARROYO J.G., VOELKEL N.F., AND BOGAARD H.J. *New Models of Pulmonary Hypertension Based on VEGF Receptor Blockade-induced Endothelial Cell Apoptosis* Pulmonary Circulation, Vol.2(4) pp. 434-442, 2012.

[40] OOI C.Y., WANG Z., TABIMA D., EICKHOFF J.C., AND CHESLER N.C. *The Role of Collagen in Extralobular Pulmonary Artery Stiffening in Response to Hypoxia-induced Pulmonary Hypertension* Am. J. Physiol. Heart Circ. Physiol, Vol.299 pp. H1823-H1831, 2010.

[41] POIANI G.J., TOZZI C.A., YOHN S.E., PIERCE R.A., BELSKY S.A., BERG R.A., YU S.Y., DEAK S.B., AND RILEY D.J. *Collagen and Elastin Metabolism in Hypertensive Pulmonary Arteries of Rats* Circulation Research, Vol.66 pp. 968-978, 1990.

[42] POLZER S., GASSER T.C., MAN V., TICHY M., SKACEL P., AND BURSA J. *Structure-based Constitutive Model Can Accurately Predict Planar Biaxial Properties of Aortic Wall Tissue* Acta Biomaterialia, Vol.14 pp. 133-145, 2014.

[43] PROSSER I.W., STENMARK K.R., SUTHAR M., CROUCH E.C., MECHAM R.P., AND PARKS W.C. *Regional Heterogeneity of Elastin and Collagen Gene Expression in Intralobar Artereis in Response to Hypoxic Pulmonary Hypertension as Demonstrated by In Situ Hybridization* American Journal of Pathology, Vol.135(6) pp. 1073-1088, 1989.

[44] PURSELL E.R., VELEZ-RENDON D., AND VALDEZ-JASSO D. *Biaxial Properties of the Left and Right Pulmonary Arteries in a Monocrotaline Rat Animal Model of Pulmonary Arterial Hypertension* J. Biomech. Engr., Vol.138(11) pp. 111004-111004-11, 2016.

[45] RAMACHANDRA A.B. AND HUMPHREY J.D. *Biomechanical Characterization of Murine Pulmonary Arteries* Journal of Biomechanics, Vol.84 pp. 18-26, 2019.

[46] RAZAVI H., ZARAFSHAR S.Y., SAWADA H., TAYLOR C.A., AND FEINSTEIN J.A. *Quantitative Characterization of Postnatal Growth Trends in Proximal Pulmonary Arteries in Rats by Phase-contrast Magnetic Resonance Imaging* Am. J. Physiol. Lung Cell Mol. Physiol. Vol.301 pp. L368-379, 2011.

[47] SCHRIEFL A.J., ZEINDLINGER G., PIERCE D.M., REGITNIG P., AND HOLZAPFEL G.A. *Determination of the Layer-specific Distributed Collagen Fibre Orientations in Human Thoracic and Abdominal Aortas and Common Iliac arteries* J. R. Soc. Interface, Vol.9 pp. 1275-1286, 2011.

[48] SICARD D., FREDENBURGH L.E., AND TSHUMPERLIN D.J. *Measured Pulmonary Arterial Tissue Stiffness is Highly Sensitive to AFM Indenter Dimension* Journal of the Mechanical Behavior of Biomedical Materials, Vol.74 pp. 118-127, 2017.

[49] STENMARK K.R., DAVIE N., FRID M., GERASIMOVSKAYA E., AND DAS M. *Role of the Adventitia in Pulmonary Vascular Remodeling* Am. Physiol. Soc., Vol.21 pp. 134-145, 2006.

[50] SUGITA S. AND MATSUMOTO T. *Multiphoton Microscopy Observations of 3D Elastin and Collagen Fiber Microstructure Changes During Pressurization in Aortic Media* Biomech. Model Mechanobiol., Vol.16 pp. 763-773, 2017.

[51] SUN W. AND CHAN S.Y. *Pulmonary Arterial Stiffness: an Early and Pervasive Driver of Pulmonary Arterial Hypertension* Frontiers in Medicine, Vol.5(204) pp. 1-8, 2018.

[52] TARASEVICIENE-STEWART L., KASAHARA Y., ALGER L., HIRTH P., MCMAHON G., WALTENBERGER J., VOELKEL N.F., AND TUDER R.M. *Inhibition of the VEGF Receptor 2 Combined With Chronic Hypoxia Causes Cell Death-dependent Pulmonary Endothelial Cell Proliferation and Severe Pulmonary Hypertension* The FASEB Journal, Vol.15 pp. 427-438, 2001.

[53] TIAN L., WANG Z., LIU Y., EICKHOFF J.C., ELICEIRI K.W., AND CHESLER N.C. *Validation of an Arterial Constitutive Model Accounting for Collagen Content and Crosslinking* Acta Biomaterialia, Vol.31 pp. 276-287, 2015.

[54] TUDER R.M. *Pulmonary Vascular Remodeling in Pulmonary Hypertension* Cell Tissue Res., Vol.367 pp. 643-649, 2017.

[55] TORTORA G.J., DERRICKSON B. *Principles of Anatomy and Physiology* 12 ed, Wiley, Hoboken, N.J., 2009

[56] TOZZI C.A, CHRISTIANSEN D.L., POIANI G.J., AND RILEY D.J. *Excess Collagen in Hypertensive Pulmonary Arteries Decreases Vascular Distensibility* Am. J. Respir. Med., Vol.149 pp. 1317-1326, 1994.

[57] VALDEZ-JASSO D., BIA D., ZOCALO Y., ARMENTANO R.L., HAIDER M.A., AND OLUFSEN M.S. *Linear and Nonlinear Viscoelastic Modeling of Aorta and Carotid Pressure-Area Dynamics Under In Vivo and Ex Vivo Conditions* Ann. Biomed. Eng., Vol 39(5) pp. 1438-1456, 2011.

[58] VELEZ-RENDON D., ZHANG X., GERRINGER J., AND VALDEZ-JASSO D. *Compensated Right Ventricular Function of the Onset of Pulmonary Hypertension in a Rat Model Depends on Chamber Remodeling and Contractile Augmentation*Pulmonary Circulation, Vol.8(4) pp. 1-13, 2018.

[59] VOELKEL N.F., GOMEZ-ARROYO J., ABBATE A., BOGAARD H.J., AND NICOLLS M.R. *Pathobiology of Pulmonary Arterial Hypertension and Right Ventricular Failure* European Respiratory Journal, Vol.40 pp. 1555-1565, 2012.

[60] WANG Z. AND CHESLER N.C. *Role of Collagen Content and Cross-linking in Large Pulmonary Arterial Stiffening After Chronic Hypoxia* Biomech Model Mechanobiology, Vol.11 pp. 279-289, 2012.

[61] WANG Z., LAKES R.S., EICKHOFF J.C, AND CHESLER N.C. *Effects of Collagen Deposition on Passive and Active Mechanical Properties of Large Pulmonary Arteries in Hypoxic Pulmonary Hypertension* Biomech Model Mechanobiology, Vol.12 pp. 1115-1125, 2013.

[62] WHITE R.J., MEOLI D.F., SWARTHOUT R.F., KALLOP D.Y., GALARIA I.I., HARVEY J.L, MILLER C.M., BLAXALL B.C., HALL C.M., PIERCE R.A., COOL C.D., AND TAUBMAN M.B. *Plexiform-like Lesions and increased Tissue Factor Expression in a Rat Model of Severe Pulmonary Hypertension* AJP-Lung Cell Mol. Physiol., Vol.293 pp. L583-L590, 2007.

[63] YU X., WANG Y, AND ZHANG Y. *Transmural Variation in Elsatin Fiber Orientation Distribution in the Arterial Wall* Journal of the Mechanical Behavior of Biomedical Materials, Vol.77 pp. 745-753, 2018.

[64] YU X., TURCOTTE R., SETA F., AND ZHANG Y. *Micromechanics of Elastic Lamellae-Unravelling the Role of Structural Inhomogeneity in Multi-Scale Arterial Mechanics* J.R. Soc. Interface, Vol. 15 pp. 1-11, 2018.